UC San Diego
UC San Diego Electronic Theses and Dissertations

Title

Automation of a Seabed Transponder Survey Using an Autonomous Surface Vehicle

Permalink

Author

Sawyer, Lauren Michelle

Publication Date

2024

Peer reviewed|Thesis/dissertation

UNIVERSITY OF CALIFORNIA SAN DIEGO

Automation of a Seabed Transponder Survey Using an Autonomous Surface Vehicle

A thesis submitted in partial satisfaction of the
requirements for the degree Masters of Science

in

Engineering Sciences (Applied Ocean Sciences)

by

Lauren Sawyer

Committee in charge:

      Mark Anderson, Co-Chair
      Sophia Merrifield, Co-Chair
      Sylvia Herbert
      Eric Terrill

2024

The Thesis of Lauren Sawyer is approved, and it is acceptable in quality and form for publication on microfilm and electronically.

University of California San Diego

2024

TABLE OF CONTENTS

LIST OF FIGURES

LIST OF TABLES

ACKNOWLEDGEMENTS

Thank you so much to Mom, Dad, and Alex for always supporting me and pushing me to take the next leap, whether that's in life or my research. This wouldn't have been possible without your guidance and love. A huge thank you to Katie for all of the 10 years of support, love, and taking on the world together. You guys are my rocks and my life is so much fuller to have you all in it.

Thank you to Mark, Sophia, and Eric for guiding me on this journey and teaching me not only how to be a scientist, but also how to be an adult and a leader. You took a huge leap of faith in taking me on as a student, and I will forever be grateful. I'm so excited to have taken these first steps in my career with you all and to do something that I am so passionate about. You three are dedicated and amazing advisors, and I always felt that you cared both about me and my education.

Finally, thank you to the CORDC lab for helping me to make San Diego my home. It's hard to move across the country, but knowing that I had a place I already belonged to made the transition so much easier. I had so many mentors to teach me about everything from research, to classwork, to life. I'm really glad that you made me feel comfortable enough to ask even the silliest questions.

<div align="center">VITA</div>

2022	Bachelor of Science, Pennsylvania State University
2022-2024	Research Assistant, University of California San Diego
2024	Masters of Science, University of California San Diego

<div align="center">PUBLICATIONS</div>

Sawyer, L., Anderson, M., Bednar, R., Merrifield, S., and Terrill, E., "Seabed Transponder Localization Behavior from an Autonomous Surface Vehicle," OCEANS 2023 - MTS/IEEE U.S. Gulf Coast, Biloxi, MS, USA, 2023. pp.1-7.
    doi: 10.23919/OCEANS52994.2023.10337356.

<div align="center">FIELDS OF STUDY</div>

Major Field: Engineering Sciences (Applied Ocean Sciences)

    Specialization in Linear and Optimal Control
    Professors S. Sakar, H. Sharma, and J. Becker

    Specialization in Fluid Mechanics
    Professors A. Lucas, O. Schmidt, and D. Saintillan

ABSTRACT OF THE THESIS

Automation of a Seabed Transponder Survey Using an Autonomous Surface Vehicle

by

Lauren Sawyer

Masters of Science in Engineering Sciences (Applied Ocean Sciences)

University of California San Diego, 2024

Mark Anderson, Co-Chair
Sophia Merrifield, Co-Chair

Knowing the transponder location for Autonomous Underwater Vehicle (AUV) navigation is imperative to predicting the location of the AUV during mission navigation. Accurate underwater navigation requires external transponder beacons or navigation aids with known locations. Traditionally, the localization method for these transponder beacons is normally done with ship-based surveys that take time and personnel. This thesis proposes that using autonomous vehicles, specifically surface vehicles, to perform the transponder survey will free up personnel, save time, and yield accurate and precise estimates of the transponder location. This thesis looks to automate the process of transponder beacon navigation.

Two approaches are applied and developed to perform localization: a least squares method and an extended Kalman Filter. These approaches are tested on field data collected by a Boeing Liquid Robotics Wave Glider equipped with a WHOI micromodem for acoustic communications and a Global Positioning System (GPS) receiver. Two field experiments were conducted in La Jolla, California in shallow water, and included varying geometries of the survey path used for localization.

The Kalman Filter outperforms the least squares method for precision, and it identifies the error bounds of the estimate. It includes a motion model specific to the physical movement of the Wave Glider's sub and float components. Finally, the Kalman filter provides an on-board algorithm that can be run in real-time without excessive usage of data storage, which the least squares method would require.

Both theoretical and data analysis conclude that traveling a 150-degree arc around the drop location will allow the area of uncertainty and transponder position covariance error ellipse to converge to a steady state value. Traveling straight line transects will also yield precise survey results and may diminish the total time it takes to perform the localization survey.

Chapter 1

Introduction

1.1 Motivation

Autonomous Underwater Vehicles (AUV) are increasingly being used in the diverse fields of ocean research. They perform various operations including passive data collection, simultaneous localization and mapping (SLAM), and tracking of other vehicles. The use of AUVs provides researchers a way to collect data and map the ocean at a lower cost than having personnel and boat time available for days on end. AUV navigation can be performed by surfacing periodically to obtain a Global Positioning System (GPS) location, then using dead-reckoning and an Inertial Navigation Systems (INS) to predict the AUV trajectory and location at a given time. However, the true location of the AUV cannot be known for certain until it surfaces again and collects another GPS position update. Surfacing is typically undesirable, as it not only increases the time it takes for the AUV to complete its mission, but it also poses a safety threat of being run over by ships or other surface vehicles.

Acoustic navigation is widely used in underwater tracking and AUV localization, especially to constrain dead reckoning navigation solutions. It is typically performed by dropping an array of acoustic transponders at known locations, then having an AUV interrogate each of the
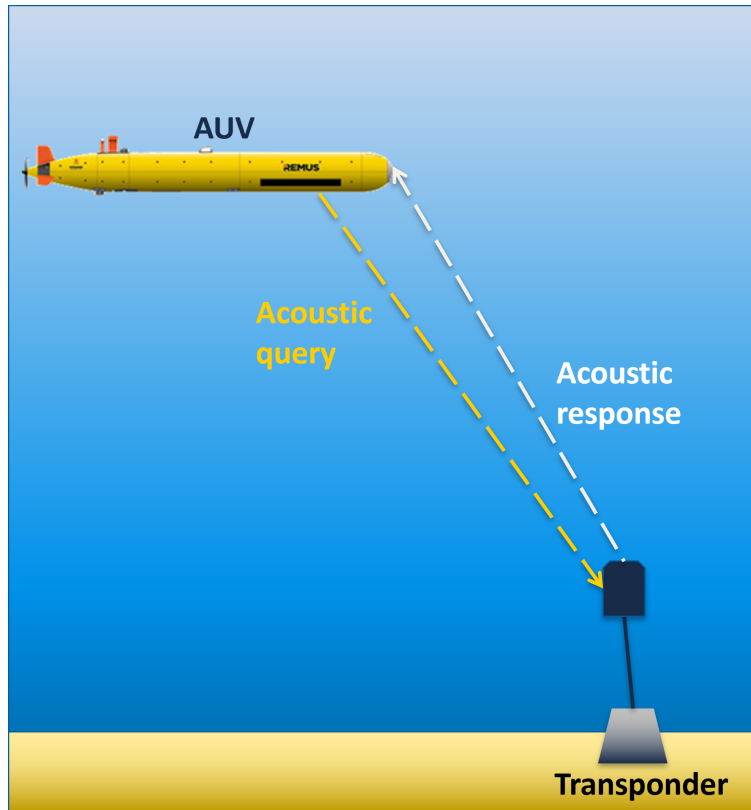
Figure 1.1. An illustrated autonomous underwater vehicle (AUV) pinging an underwater transponder for the use of underwater navigation

transponders, and finally receiving the transponder response (as seen in Figure 1.1). The range is

calculated from the AUV to the transponder using the one-way travel time (OWTT) signal of the

response and the known speed of sound in water. The assembled range measurements from each

transponder allows the AUV to localize itself with respect to the array of known transponder

locations. However, in order to reduce cost, the use of single-transponder acoustic navigation has

been used more recently in AUV missions. These typically provide less accuracy than multiple

transponders would, but reduce the amount of deployment/retrieval time, as well as the surveys

necessary to precisely locate each of the transponders.

The GPS location of the operations boat, when dropping the transponder, is typically

accurate. However, a large position uncertainty may result because the actual drift and landing location of the transponder is unknown until it is localized through post-deployment surveys. The location of an AUV underwater is only as precise as the transponder location that is acting as the baseline, so it is crucial to know these transponder coordinates for precise AUV navigation [1]. These surveys are often performed by ships, which can only yield a final transponder location with 7 to 10 meters of uncertainty in any direction [2]. Further, ship surveys are time consuming, costly, and have low maneuverability. Thus, the use of Autonomous Surface Vehicles (ASV) is being examined for these surveys to ultimately save money and yield a more precise and accurate fix on the transponder location.

The advantages an ASV poses to the localization survey are that it can be highly maneuverable, it moves at much lower speeds than a ship (thus yielding less uncertainty in the range measurement), and that it can be equipped with on-board processing of the measurements to yield the transponder location results in real time, even communicating the location instantly with an AUV that is present in the area. The use of an ASV to survey the transponder frees the survey ship and its personnel for other tasks, and the high maneuverability of the ASV potentially means that a traditional, full-circle area survey may not be necessary. This paper will examine if there is a relationship between the accuracy of the final location estimation and the distance traveled around the survey circle. Given this relationship, the ASV can determine if it can abandon the survey track once it is confident in its assessment of the transponder location. This study therefore seeks to determine how the length of the survey circle affects the precision and accuracy of the resulting transponder location.

1.2   Previous Work

Previous work has been done to improve surveys with the use of an ASV, specifically a Liquid Robotics Wave Glider. Further, using only a single transponder instead of an array is being considered, especially by Masmitja in 2018 [3] and Xie in 2022 [4]. Xie considers applying single transponder navigation in shallow water applications and reports centimeter accuracy in the horizontal plane estimate of the transponder [4]. Masmitja analyzes, through simulation and field tests, how the path of the ASV can effectively reduce uncertainty in the estimate by relating an optimal survey path to the accuracy of the estimate obtained [3].

Studies have also investigated methods of filtering noisy data to ensure that an accurate prediction is achieved. Typical methods of noise filtering include a priori information on the transponder location and using periods of consistent measurement to filter outlier data [5]. Olsen's study in 2006 proposes spectral graph partitioning, while this paper proposes integrating the noise filtering algorithm within the Kalman filter [5].

These works provide a strong foundation for the work done in this paper, especially noting that a survey centered around the transponder drop point appears to be the optimal approach [3]. However, this paper also seeks to not only quantify the specific relationship between precision and the path of the survey, but also to yield a localization algorithm that can be employed on board the ASV. Least-squares methods are traditionally employed in these surveys to yield the transponder location estimate [3]. This paper will begin with a least-squares method analysis, and then move to design a Kalman filter and motion model specific to the Wave Glider in order to effectively compute the transponder location in real time.

1.2.1 Applications to Geodesy

There have also been some previous studies looking into the use of a Wave Glider to perform geodetic surveys. Spiess, in his 1985 and 1998 papers, lays the groundwork for acoustic surveys to obtain centimeter-scale accuracy [6] [7]. Spiess' work is the fundamental basis for the survey performed in this experiment, using a transponder for acoustic ranging and a GPS receiver to synchronize clocks on the vehicle. However, both Spiess [6] and Send [8] also suggest the use of multiple transponders to increase accuracy, while this study only looks at the use of a single transponder to ease the deployment load. The works of Chadwell (2016) [9] and Iinuma (2021) [10] also use a Wave Glider to perform surveys that measure crust deformation and seafloor motion. These works conclude that centimeter-scale accuracy is possible in identifying a transponder's location. These surveys can take as short as five days and as long as one month to achieve this kind of precision and accuracy for the final location estimation.

Centimeter-scale accuracy is ideal when monitoring the slow, decadal movement of the seafloor. However, when AUV missions themselves take less than a week, a transponder survey that takes at least five days is unjustified. Thus, this paper seeks to balance the available time that the transponder survey has allotted, with the desired accuracy of the transponder location, as dependent on the specific mission being run by the AUV. This paper will seek to establish a relationship between the path of a survey around a transponder and the subsequent accuracy that the survey yields in its transponder position estimate. Thus, the transponder survey can become a relatively quick, few hour transit that establishes the transponder location without the need for extra personnel.

1.3   Wave Glider ASV

This study was performed using a Boeing Liquid Robotics Inc. Wave Glider SV3-v300 (seen in Fig. 1.2) to accomplish the transponder survey used as the primary data set. The Wave Glider is equipped with a sub-surface component comprising of a Woods Hole Oceanographic Institute (WHOI) acoustic communications (ACOMMS) payload configured to operate at 25 kHz. Two WHOI Micro-modem v2's drive undersea communications at both 10 and 25 kHz, and are integrated with a WHOI acceleration-canceling array. The equipment allows the Wave Glider to communicate with other micro-modems, as well as to ping various transponder devices and compute the OWTT responses [11]. The OWTT calculation factors in the turn-around time (TAT) of a transponder's internal "ping reply processing time", and then divides the total travel time by two. The preset TAT of 50 milliseconds is constant and configured as a parameter within the Micro-modem, given that the 25 kHz transponder lists this number as its internal processing time. The float component of the Wave Glider is equipped with a GPS receiver that remains above water at all times to ensure accurate position fixes [12]. The GPS receiver provides new measurements at a frequency of 1 Hz. It receives measurements from an antenna located on top of the most forward vertical sensor column seen in Fig. 1.2.

1.4   Data Sets

1.4.1   December 2022 Data Collection

The data set was collected offshore of La Jolla, California (seen in Fig. 1.3). The Wave Glider performs an almost complete circle around the transponder drop location, resulting in the data set illustrated in Fig. 1.4. It receives GPS fixes at a rate of 1 Hz, and samples the

6

Figure 1.2. The Wave Glider is seen prepped for deployment. Top component is the float, and the sub is beneath it attached to an umbilical (not pictured). The 25 kHz transducer is below the sub component towards the aft rudder and underside of the vehicle. The bottom picture is a zoom-in on the sub and transducer
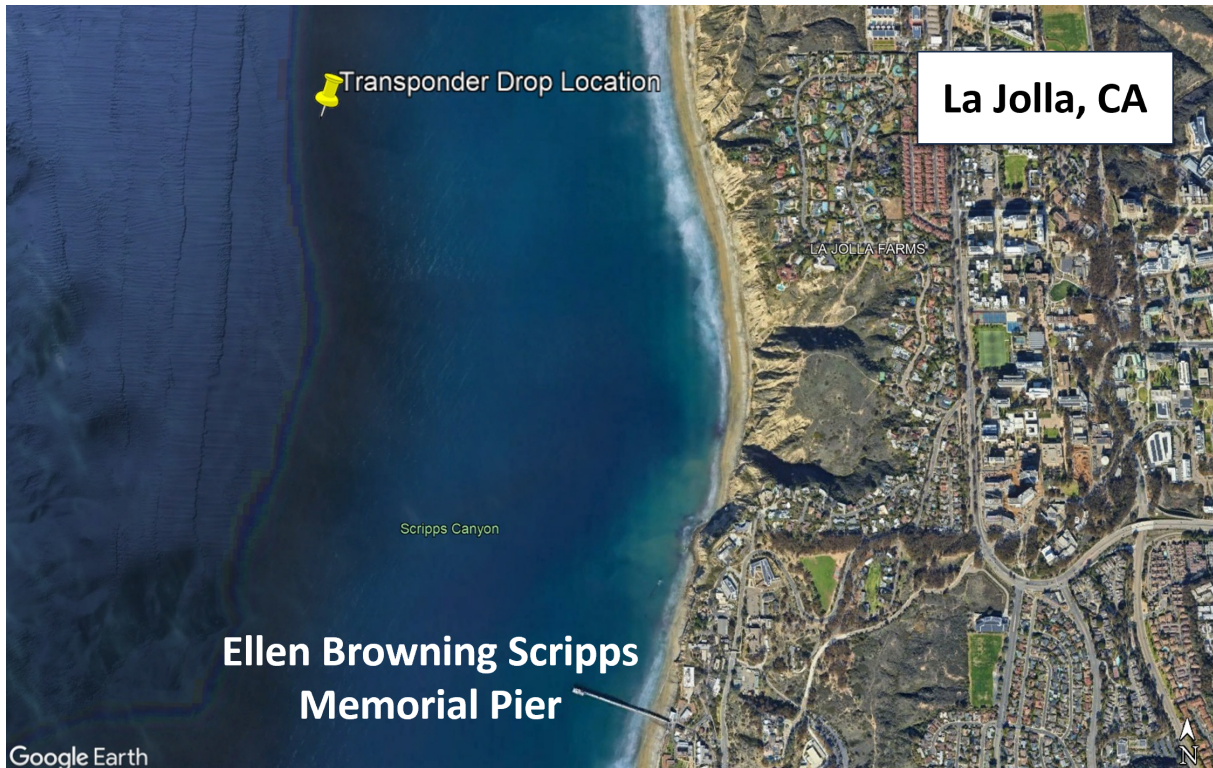
Figure 1.3. Planned drop location of transponder for Dec. 2022 experiment

transponder at a rate of 0.1 Hz. The Wave Glider's GPS receiver is a UBLOX-NEO-M8U model. Further, the vehicle moves at a relatively constant speed of less than 1 m/s, so it does not move a considerable distance between querying the transponder and receiving the response. The depth of the transponder at the survey location was 11 meters, and the 25 kHz BT-2 transducer resides at the end of the umbilical connecting the sub to the float, at 8.5 meters depth. Therefore, the vertical depth the acoustic ping must travel is only 2.5 meters, while the horizontal distance is on the order of 150 meters, as seen in Fig. 1.4. The assumption is made for the remainder of this paper that, because depth is negligible in comparison to the direct travel distance, the geometry can be considered two-dimensional. Further support for this assumption is that the transponder is anchored to the sea floor, so its depth and the depth of the Wave Glider's tow will remain constant with all of the measurements.
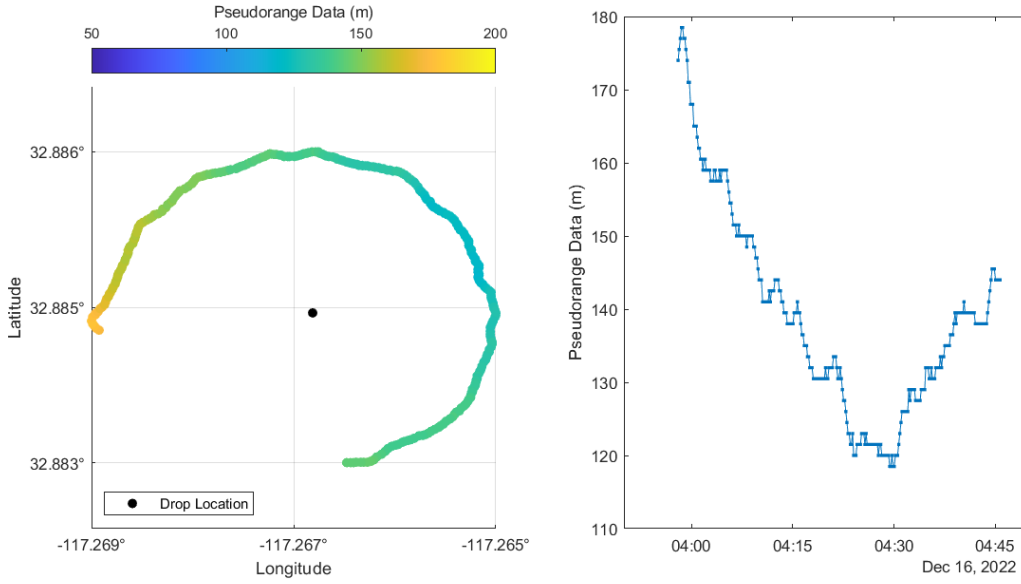
Figure 1.4. Left: Path of transponder survey. Survey started at the west end and proceeds clockwise around the circle. Right: Travel time measurements converted to pseudoranges. Drop location denoted by black dot.

The one-way travel time measurements, collected by the ASV, are shown in Fig. 1.4. These 287 raw time measurements are converted to range measurements using Eq. (1.1). This process requires the speed of sound in water, which must be calculated for the location and time that the survey took place. The nine term Mackenzie equation is used with temperature and salinity measurements that were acquired from a CTD (Conductivity, Temperature, Depth) profiler at a nearby moored buoy during the time period that the survey was performed [13]. It is assumed that the speed of sound remains constant both spatially and temporally for this study.

$$d_k = OWTT_k * c_{sound\ in\ water} \tag{1.1}$$

The speed of sound is assumed spatially constant throughout the water column in this application due to the short vertical distance the acoustic waves travel. From Fig. 1.5 it is evident

9
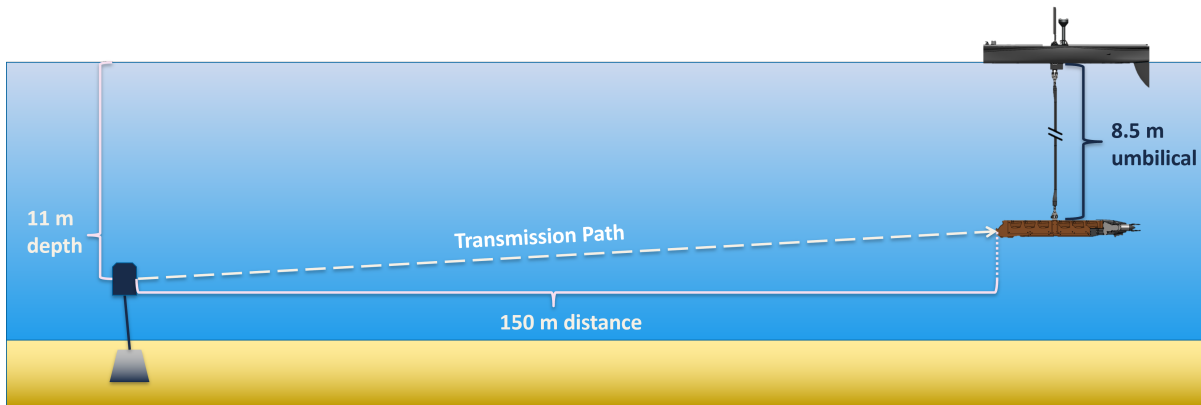
Figure 1.5. Sketch of vertical profile of Wave Glider in water with transponder at 11 meters depth

that there is only a 2.5-meter vertical distance between the transducer and the transponder. The temperature and salinity are also assumed to remain constant throughout the duration of the survey. While this is a good assumption for this particular survey setup, the speed of sound may not be constant in deeper water columns where there is a distinct thermocline that the acoustic wave must travel through. Thus, a variable speed of sound may need to be accounted for in future tests and applications.

Another inherent uncertainty in the sensors is the difference in the duty cycles between the GPS sensor and the micro-modem. This analysis assumes that when a range is received by the micro-modem, the GPS location of the Wave Glider is taken simultaneously. The micro-modem calls for a range reading every 10 seconds, but this may not necessarily align with the GPS reading that is received every one second. The Wave Glider may travel between the last GPS reading and the micro-modem range reading, yielding an uncertainty of no more than a few meters. The position of the actual transducer on the sub component is unknown relative to the acquired GPS location, which could potentially introduce another one to three meters of

uncertainty. Further, the variance of the micro-modem's arrival sensor is approximately 0.2 milliseconds, which would translate into an additional uncertainty of 0.3 meters. This study will show that the geometry of the survey can either exacerbate this error or help to attenuate it.

1.4.2   August 2023 Experiment Design

While the first data set was useful in creating a preliminary algorithm, a new question was posed about how the geometry or shape of the survey conducted around the transponder would affect the accuracy of the transponder location prediction. This new experiment implemented a half-square survey shape, or an "L-shaped" survey, to explore if straight line transects could provide an equally precise estimate of the transponder location. The experiment was designed to replicate many of the parameters of the first December 2022 dataset, such as the transponder drop location, the frequency of communication between the transponder and the ASV, and the GPS sensors used to track the ASV location throughout each run. The idea of increasing the distance from 150 meters to 1 kilometer was intended to determine if an accurate estimate could be generated by simply performing a "drive-by" maneuver. The L-shape was also chosen because, based on the analysis in Chapter 2.5, traveling the equivalent of a semi-circle around the transponder should be enough to capture an accurate and precise location estimate. Similarly, two legs of a square shape should be enough to capture an accurate prediction. The track for the L-shape test can be seen in Figure 1.6. It will also be analyzed how using one leg of the L-shape versus both legs affects the final position estimate of the transponder and its associated covariance ellipse.

It is also clear from Figure 1.6 that there are more outlier pseudoranges recorded from this dataset than the previous data set collected in December 2022. This difference is attributed to
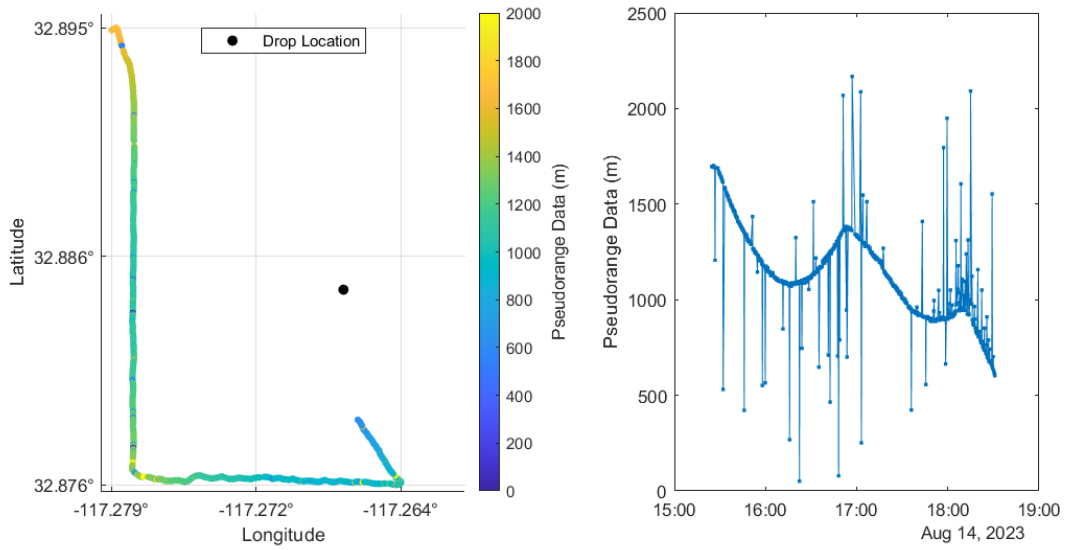
Figure 1.6. Left: Path of L-survey performed by Wave Glider. The color variable indicates the pseudorange measurements received at each location. Right: Travel time measurements converted to pseudorange.

the settings of the signal to noise ratio threshold on the acoustic modem. Because the threshold was set lower than the setting from December 2022, there was more opportunity for multipath signals or delayed time of arrival to be recorded. The setting was changed because the ASV was running long distance communications during testing week and, due to the attenuation of sound traveling over distance, the acoustic signal was weaker when it arrived at the ASV. In the December 2022 experiment, the signal had less distance over which it could attenuate, and thus the signal to noise ratio threshold could be set higher.

The drop location seen in Figure 1.7 was chosen in part to recreate many of the physical conditions from the December 2022 experiment. However, due to the large transect of the L-shape and the surrounding bathymetry, the location had to be shifted slightly to ensure that the ASV did not travel in an area shallower than 18 meters. Thus, the final depth for the transponder in the August survey was approximately 30 meters to the seafloor.
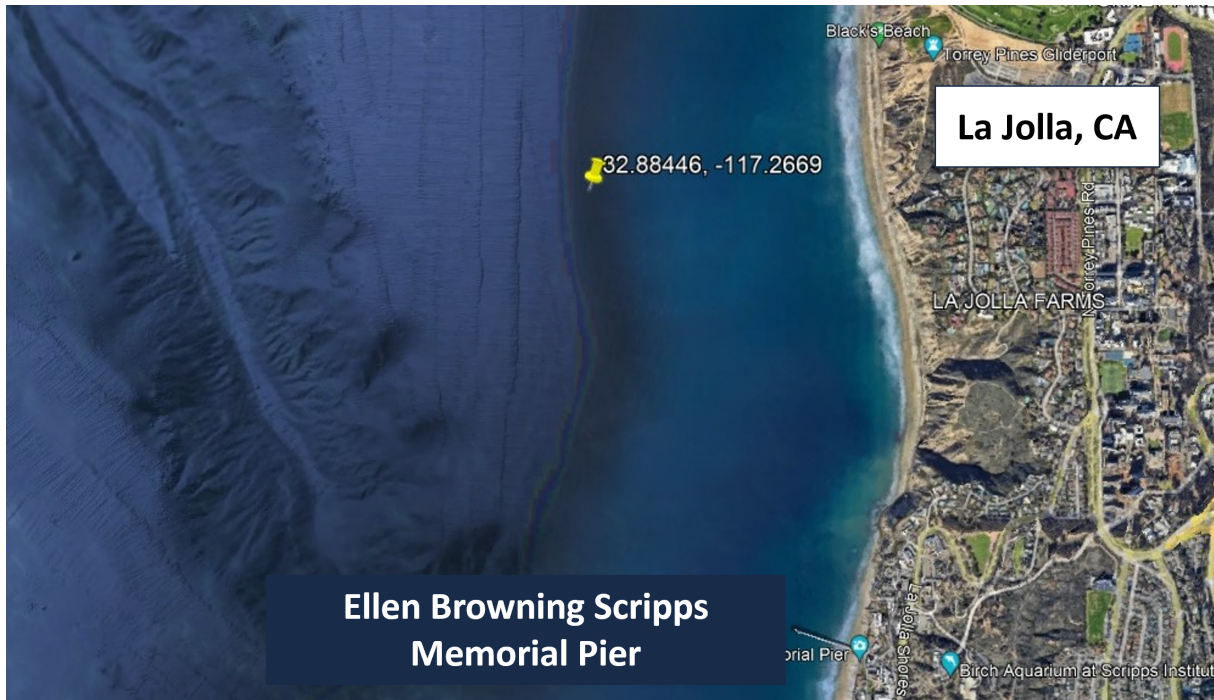
Figure 1.7. Planned drop location of transponder for August 2023 experiment

1.4.3   Environment Conditions During Data Collection

CTD (conductivity, temperature, and depth) casts were also taken on four out of the six days of testing to determine a speed of sound profile for the water column during the August 2023 data set collection. It was determined that a sound speed of c = 1495 m/s would be used for the distance calculations in Equation 1.1 whenever the August 2023 data set is used in the analysis. Speed of sound figures from the CTD casts can be found in the Appendix. No CTD casts were taken when the December 2022 data was collected, so local temperature and salinity data was taken from a nearby mooring. The speed of sound used for the December 2022 data analysis was c = 1500 m/s.

Forward propulsion of the Wave Glider depends on the sea state and ocean currents [14] [15]. The wave height and period play a significant role in the behavior and physical motion of

13

the Wave Glider. The bulk parameters for each experiment for the December 2022 and August 2023 experiments, respectively, give insight as to how the Wave Glider was propagating during each of the individual survey runs. Larger significant wave heights translate into the Wave Glider traveling at higher velocities, as it is using the available wave energy to propel its forward motion. The significant wave height during each testing period was less than a meter high. Thus, the velocity of the Wave Glider will be small (less than 1 m/s), and the motion of the umbilical can be assumed to have consistent oscillations throughout each experiment. Peak velocity of the Wave Glider for both experiments was 0.5 m/s.

Chapter 2

Theoretical Models and Least-Squares Analysis

2.1 Position Solution for Dec. 2022 Data Set

The first method used to solve the transponder position was a least-squares method. This method was chosen because it is the standard method used in ship transponder surveys [8]. The least-squares method uses only the one-way travel time and the position of the Wave Glider at each acoustic response to compose the range equation. Because the least-squares method requires an over-determined system, at least four different acoustic one-way travel time responses are required. The least-squares approach is also amenable to either batch or recursive implementations. The general solution of this method will be presented first in the next section, and then the subsequent sections will apply that general solution to a specific, theoretical case that assumes the radial distance from the ASV to the stationary transponder remains constant. This special case leads to an analysis of precision dependent on the degrees of the survey arc traveled, and it will lead to a closed-form solution for the dilution of precision. The dilution of precision proves an assessment of the limits of precision for this estimate.

15

2.1.1 Least-Squares Solution

The position measurements taken by the GPS receiver on the ASV are provided in the form of latitude and longitude angles. However, angular measurements in degrees, minutes, and seconds are difficult to use in mathematical manipulations. Thus, the position data must be converted into a local Cartesian frame of reference to ease the mathematical processing. The geodetic coordinates of each individual ASV location are converted into x (north) and y (east) coordinates, with the origin of this local frame set to the known transponder drop location. The drop location was chosen as the reference origin due to its central location to the subsequent surveys, as well as because the final transponder location should end up near the origin. The conversion expressions are given by Eqs. (2.1) and (2.2), which assume a spherical Earth, with ϕ as latitude, λ as longitude, and R_E as the Earth radius.

$$x = R_E(\phi - \phi_{ref}) \tag{2.1}$$

$$y = R_E \cos \phi (\lambda - \lambda_{ref}) \tag{2.2}$$

The range equation, shown in Eq. (2.3), is then applied to each individual measurement. The variables x_0 and y_0 in this equation represent the unknown north and east coordinates of the transponder, respectively. Because the transponder is bottom mounted, there is little variation in its position due to the currents and wave motion; thus, x_0 and y_0 are assumed to be constants. The variables x_k and y_k denote the position location of the ASV platform, given by the GPS, at time index $k = 1, .., N$. The variable d_k represents the pseudorange distance, calculated from

16

the measured one-way travel time response of the acoustic message, between the ASV and

transponder at time index k. Finally, the z component is a constant value that is obtained by

subtracting the depth of the drop site from the 8.5 meter umbilical that houses the acoustic

transducer on the ASV. It is assumed that the variations in the depth of this umbilical are zero

mean noise, and thus the z_{depth} value is a single, constant value.

$$(x_k - x_0)^2 + (y_k - y_0)^2 + z_{depth}^2 = d_k^2 \tag{2.3}$$

The least-squares method requires a linear physical model to transform the equations into

a system of matrices. A linear expression is obtained by subtracting each range equation from

individual measurements from a reference range equation [16]. If the first survey point and its

subsequent range equation are taken as the reference, then all remaining measurement equations

can be subtracted from it, resulting in Eq. (2.4). This equation is now linear with respect to the

unknown transponder position location. Equation (2.4) provides $i = 2, .., N$ expressions for the

least-squares solution formulation.

$$x_i^2 - 2x_0(x_i - x_1) - x_1^2 + y_i^2 - 2y_0(y_i - y_1) - y_1^2 = d_i^2 - d_1^2 \tag{2.4}$$

The collection of differenced measurements forms a linear system, as seen in Eq. (2.5).

The two components of the unknown transducer position are included in the vector χ. The

system matrix A is constructed from the known position of the ASV platform. The vector b

includes a combination of the measured travel time and associated pseudoranges, as well as the

measured platform position variables.

$$A\chi = b \tag{2.5}$$

$$A = \begin{bmatrix} x_1 - x_2 & y_1 - y_2 \\ x_1 - x_3 & y_1 - y_3 \\ \vdots & \vdots \\ x_1 - x_N & y_1 - y_N \end{bmatrix}$$

$$\chi = \begin{bmatrix} x_0 \\ y_0 \end{bmatrix}$$

$$b = \begin{bmatrix} \frac{1}{2}(d_2^2 - d_1^2 + x_1^2 - x_2^2 + y_1^2 - y_2^2) \\ \frac{1}{2}(d_3^2 - d_1^2 + x_1^2 - x_3^2 + y_1^2 - y_3^2) \\ \vdots \\ \frac{1}{2}(d_N^2 - d_1^2 + x_1^2 - x_N^2 + y_1^2 - y_N^2) \end{bmatrix}$$

The least-squares solution seeks to minimize the mean squared error in the over-determined linear system [17]. Eq. (2.6) yields the best solution for the unknown vector χ, thus yielding the estimated position of the transponder.

$$\bar{\chi} = (A^T A)^{-1} A^T b \tag{2.6}$$

2.2 Transducer Position Error

A random error n_k is added to the calculated pseudoranges to represent uncertainty in modem message timing. Squaring the pseudorange leads to Eq. (2.7). Following Ref. [17], it is further assumed that the distance errors are small in magnitude so that the squared error can be neglected. Equation (2.8) is then applied to the difference between measurement $k = i$ and the first survey measurement $k = 1$ to yield Eq. (2.9)

$$(d_k + n_k)^2 = d_k^2 + 2d_k n_k + n_k^2 \tag{2.7}$$

$$(d_k + n_k)^2 \approx d_k^2 + 2d_k n_k \tag{2.8}$$

$$(d_i + n_i)^2 - (d_1 + n_1)^2 = d_i^2 - d_1^2 + 2(d_i n_i - d_1 n_1) \tag{2.9}$$

As illustrated in Fig. 1.4, the distances d_i and d_1 will be similar in magnitude throughout the transponder survey. Consequently, the contributions of the random distance errors can be similarly scaled, with R representing the scale factor. The linear system, with distance error, is given as Eq. (2.11), where ε represents a vector of error differences, $\varepsilon_i = n_i - n_1$.

$$(d_i + n_i)^2 - (d_1 + n_1)^2 = d_i^2 - d_1^2 + 2R(n_i - n_1) \tag{2.10}$$

$$A\chi = b + R\varepsilon \tag{2.11}$$

19

Equation (2.12) provides the covariance matrix of the error vector if the distance errors are independent in time, zero-mean, and with variance equal to σ^2. The transducer position error covariance Ξ is then found as Eq. (2.13).

$$E[R\varepsilon(R\varepsilon)^T] = 2\sigma^2 R^2 I \tag{2.12}$$

$$\Xi = E[(\chi - \bar{\chi})(\chi - \bar{\chi})^T] = 2\sigma^2 R^2 (A^T A)^{-1} \tag{2.13}$$

The diagonal elements of Ξ yield the transducer position error variance in the north and east directions. The square root of diagonal elements' sum provides a measure of the overall precision of the least-squares solution subjected to the random distance measurement errors. Eq. (2.13) demonstrates that the position error variance is proportional to the variance of the distance measurement errors. This proportionality constant is generally referred to as the "dilution of precision" or DOP. Consequently, HDOP, or the horizontal dilution of precision, can be computed directly from Eq. (2.13). The resulting expressions are given as Eqs. (2.14) and (2.15).

$$\sqrt{tr[\Xi]} = HDOP * \sigma \tag{2.14}$$

$$HDOP = R\sqrt{2\,tr[(A^T A)^{-1}]} \tag{2.15}$$

2.2.1 Solution Geometry

Dilution of precision is widely used to quantify the expected precision of reported GPS user positions [18]. It is a unitless number that is multiplied by the sensor measurement error to represent how a certain constellation of satellites positively or negatively affects the final position estimate of the user. Related literature suggests that HDOP values less than two indicate that a GPS solution is trustworthy [19]. HDOP for the transducer survey problem is similar to HDOP in GPS as both provide insight into how the measurement node geometry affects the resulting position solution [20]. In this case, HDOP is used to assess how the "constellation" of the ASV positions around the survey circle will affect the overall precision of the transponder estimate. The effect of the survey arc length on the precision of the final position estimate will be analyzed.

The transducer position solution, developed for this application, is a two-dimensional problem with two unknowns. Therefore, a minimum of three measurements are required to obtain a unique solution and a fully determined system of matrix equations [16]. To investigate how HDOP affects the resulting transducer position solution, a theoretical problem is constructed by setting three points on the circumference of a circle with constant radius R. These three points represent the position of the ASV platform receiving an acoustic response at three different moments in time.

It will be assumed that the measurement points are evenly spaced around the circle with an arc length of θ between points 1 and 2, and similarly, between points 2 and 3 (see Fig. 2.1). Consequently, the ASV has circumscribed a total arc length of 2θ during the survey. The locations of the ASV at the three measurement points are expressed in Eq. (2.16), where the first point is set due north of the circular survey center.
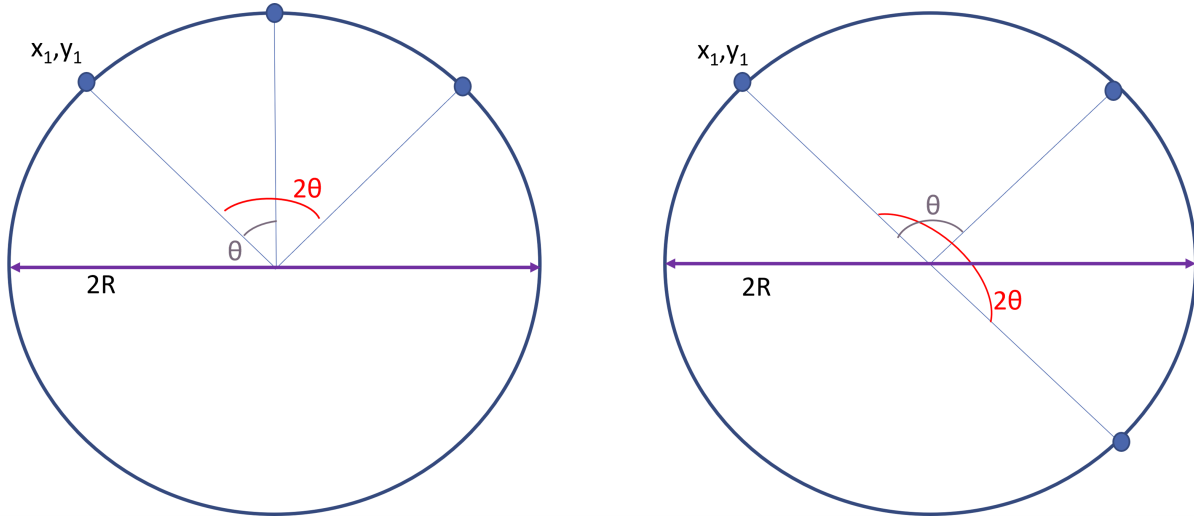
Figure 2.1. Illustration examples of two configurations with evenly spaced survey points

$$\begin{bmatrix} x_1 \\ y_1 \end{bmatrix} = \begin{bmatrix} R \\ 0 \end{bmatrix}, \begin{bmatrix} x_2 \\ y_2 \end{bmatrix} = \begin{bmatrix} R\cos\theta \\ R\sin\theta \end{bmatrix}, \begin{bmatrix} x_3 \\ y_3 \end{bmatrix} = \begin{bmatrix} R\cos 2\theta \\ R\sin 2\theta \end{bmatrix} \tag{2.16}$$

The system matrix A, given in (2.5), is then constructed with the positions of the three

points, yielding the matrix given in (2.17). Equation (2.17) is then substituted into Eq. (2.15) to

yield Eq. (2.18). Note that the radius term R cancels throughout the calculation, revealing that

HDOP is only a function θ, a measure of how far around the survey circle the ASV has traveled.

$$A = R \begin{bmatrix} 1 - \cos\theta & -\sin\theta \\ 1 - \cos 2\theta & -\sin 2\theta \end{bmatrix} \tag{2.17}$$

$$\text{HDOP} = \frac{\sqrt{2 - \cos\theta - \cos 2\theta}}{\sin\theta(1 - \cos\theta)} \tag{2.18}$$

Figure 2.2 graphs the HDOP function, as determined by Eq. (2.18), against the total

survey arc length 2θ. A very small arc traveled results in a high HDOP value, indicating that the

transponder position solution is greatly affected by the poor geometric resolution of the three measurement points. HDOP then decreases rapidly as the survey arc length increases. HDOP continues at low values until a discontinuity is reached at $2\theta = 360°$. This discontinuity results because a 360 degree total survey arc means the ASV is positioned at a location due north for both its first and last measurement. Clearly this arc represents a poor solution geometry as it implies that there are only two unique range distance measurements available for the solution.

HDOP is minimized after an approximate arc of $2\theta = 150°$ is reached, and it drops below 2 at 150°. This result suggests that an arc of at least 150° must be driven around a transponder to achieve a precise fix on its location. To illustrate how the position error covariance matrix shrinks with increasing arc length, two values for the HDOP were chosen to plot the geometric configurations of the survey points and the resulting 86% probability error ellipses. Fig. 2.3 shows that the narrower arc results in a large error ellipse due to its large HDOP value, while a much larger arc traveled (and thus a higher value of 2θ) has a low HDOP and therefore a small error ellipse.

The actual size of the transponder position error ellipse, for a given survey, will depend on the range distance between the glider and the transponder. A survey radius of 50 meters was used to create Fig. 2.3. Thus it is clear that HDOP and precision are closely tied, and larger survey arc leads directly to a better precision of the transponder location estimate.

This result can also be applied to determine if it is fully necessary to drive a complete circle around a transponder for a precise survey, or if only a partial circular arc may be taken. Since the HDOP only changes in minuscule increments after an arc of 150°, the theory suggests that only traveling about 40% of a circle yields approximately the same precision in the final
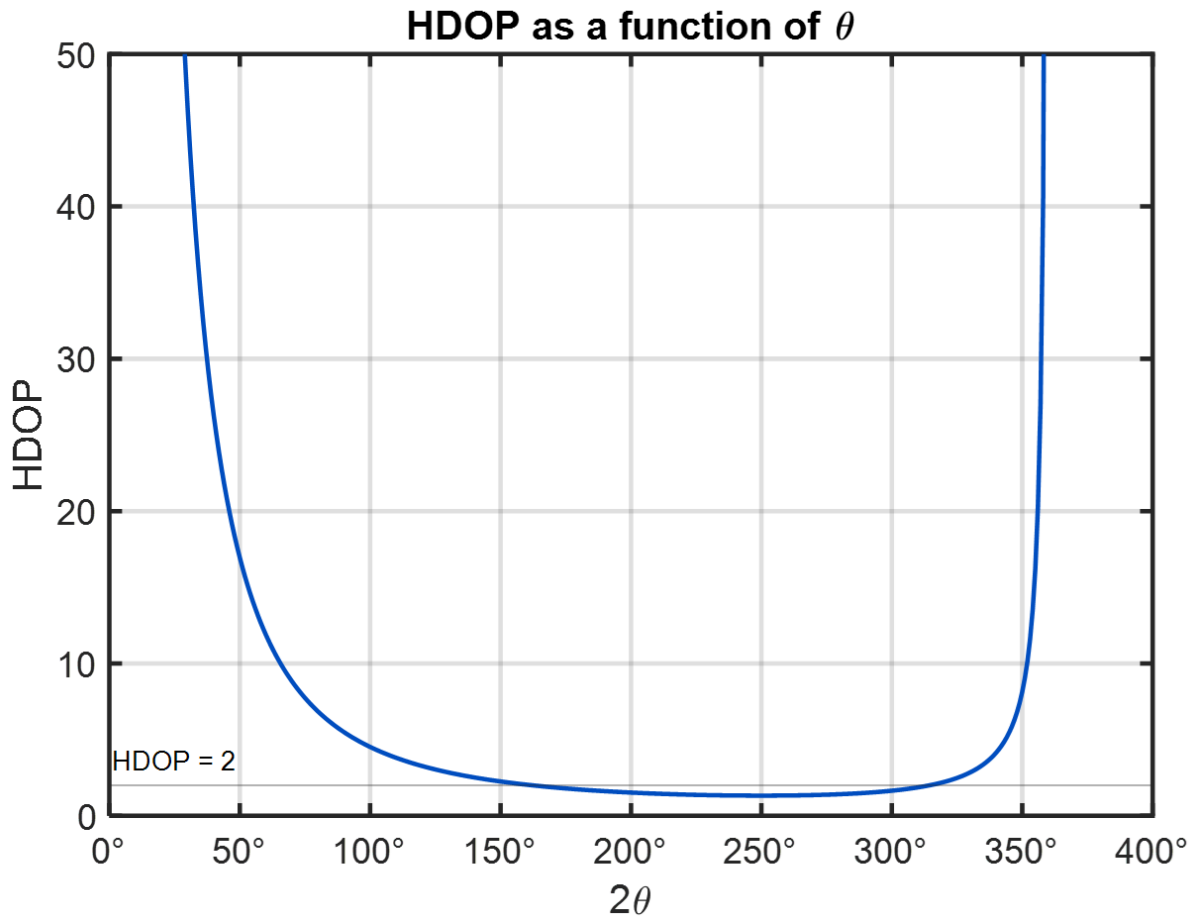
Figure 2.2. Theoretical HDOP as a function of arc length (2θ).

estimation as traveling the full circle during a survey.

A theoretical analysis has shown that a minimum arc of $150°$ must be traveled around the transponder to yield a HDOP value that indicates high precision. This result will be compared with results obtained from the the sample data set in the next section.

2.3   Least-Squares Solution on Dec. 2022 Data Set

For the rest of this study, the least-squares solution, using all 287 available measurements, will serve as the "ground truth", or the actual location of the transponder, and it can be seen with respect to the drop location in Fig. 2.4. This assumption is made because the exact position of
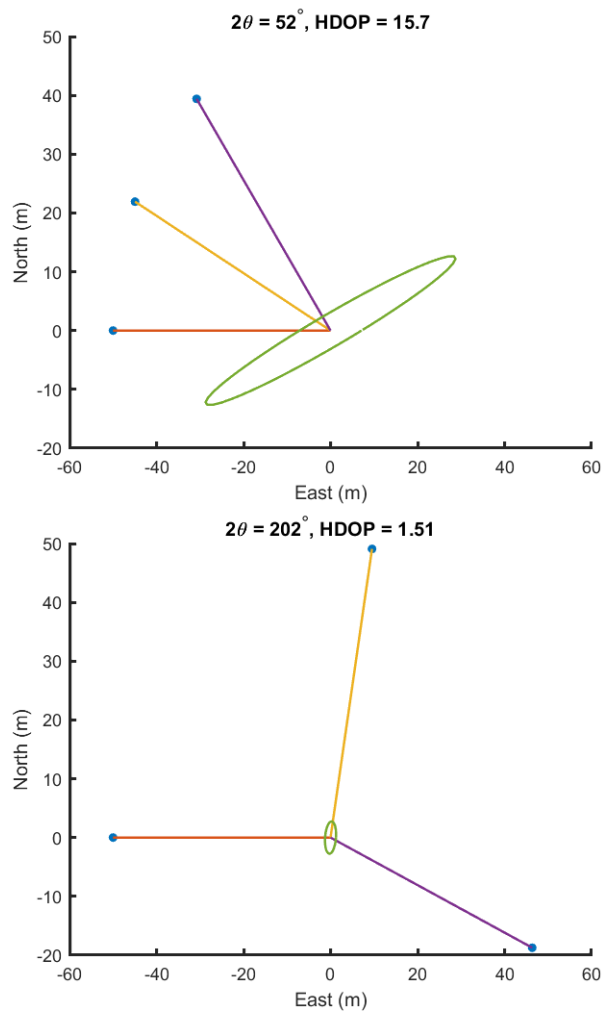
Figure 2.3. Two different HDOP values plotted to analyze their geometry and the associated error ellipse. Top: Narrow geometry with large error ellipse. Bottom: Spread out geometry with small error ellipse.

25
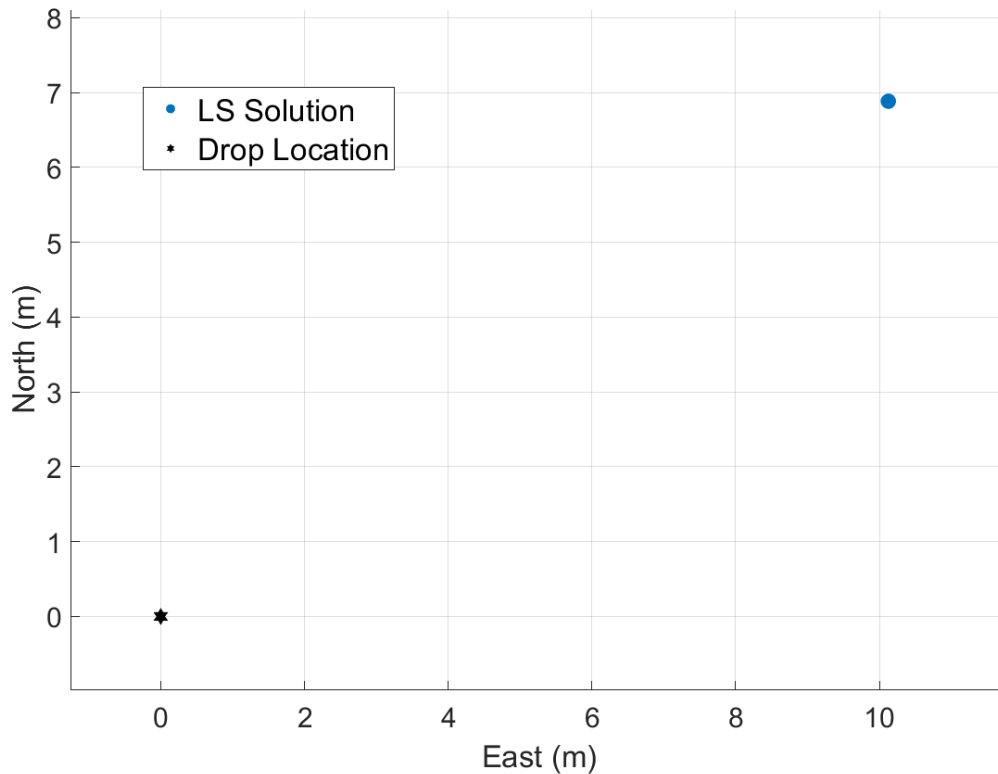
Figure 2.4. December 2022 Least-Squares Solution with all 287 points.

the transponder during this survey is not known with a high degree of certainty. Finding the least-squares solution recursively illustrates how the survey arc length affects solution accuracy. As more survey points are considered within the least-squares solution, the uncertainty range around the location estimate diminishes towards zero in both the north and east directions, as seen in Fig. 2.5. As the arc around the circle increases, HDOP decreases in amplitude along with the size of the transponder position error covariance matrix. This result confirms that a larger arc will increase the overall precision of the survey results.

The error bars in Figure 2.5 represent the 95% probability level for the north and east position variance. The error bars are seen to collapse to a very small level as the arc length approaches 150 degrees. There is very little noticeable difference in the amplitude of the variance
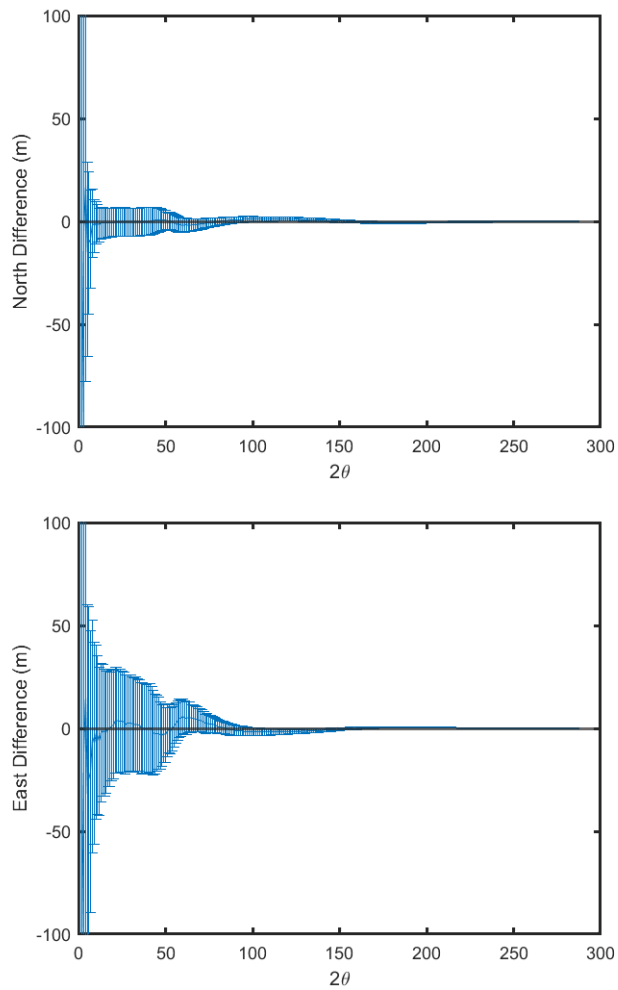
Figure 2.5. Difference between solutions for arc of 2θ points versus the "ground truth". Error bars are calculated using the covariance matrix obtained for each A matrix, then multiplied by 2 to give a 2σ or 95% probability level. Top: Error in north direction. Bottom: Error in the east direction.

at arc lengths beyond this value. It is also worth noting that the error bars do not reliably encompass the ground truth full measurement least-squares solution. This trend likely results from the fact that the position error covariance is computed assuming the only random error is caused by modem timing measurements. Uncertainty resulting from imprecise location reports from the ASV will be a focus in Chapter 3.4.

2.3.1   Evenly Spaced Survey Points

The sample data set can also be used to confirm trends noted in the theoretical study of the three-measurement solution, as described in Section 2.1. This example removes the restriction of a constant radius survey circle, by choosing three points around the actual ASV survey. The first measurement is chosen as the first survey point and the remaining two measurement points are selected to yield even spacing of arc θ (simlar to the theoretical analysis). The algorithm uses the three selected points to calculate the least-squares solution to the transponder location. It then compares this solution to the "ground truth" transponder location calculated with all 287 survey points. It can be seen in Figure 2.6 that the HDOP value converges to a constant between a 2θ value of 150 and 200 degrees, which coincides with the mathematical analysis of the HDOP equation (Eq. 2.18) displayed in Figure 2.2

In Fig. 2.6, the HDOP value dips below 2 at an arc length of $150°$, and minimizes to convergence at a $200°$ arc. HDOP is calculated by using ASV position values of the selected survey points using Eq. (2.15). The results from the data for an evenly-spaced solution set align well with the theoretical solution from Section 2.1. This data-driven study confirms that, to obtain maximum precision, a survey arc of at least $150°$ to $200°$ should be driven around the transponder, which agrees with the theoretical geometric analysis prediction of the survey arc. To
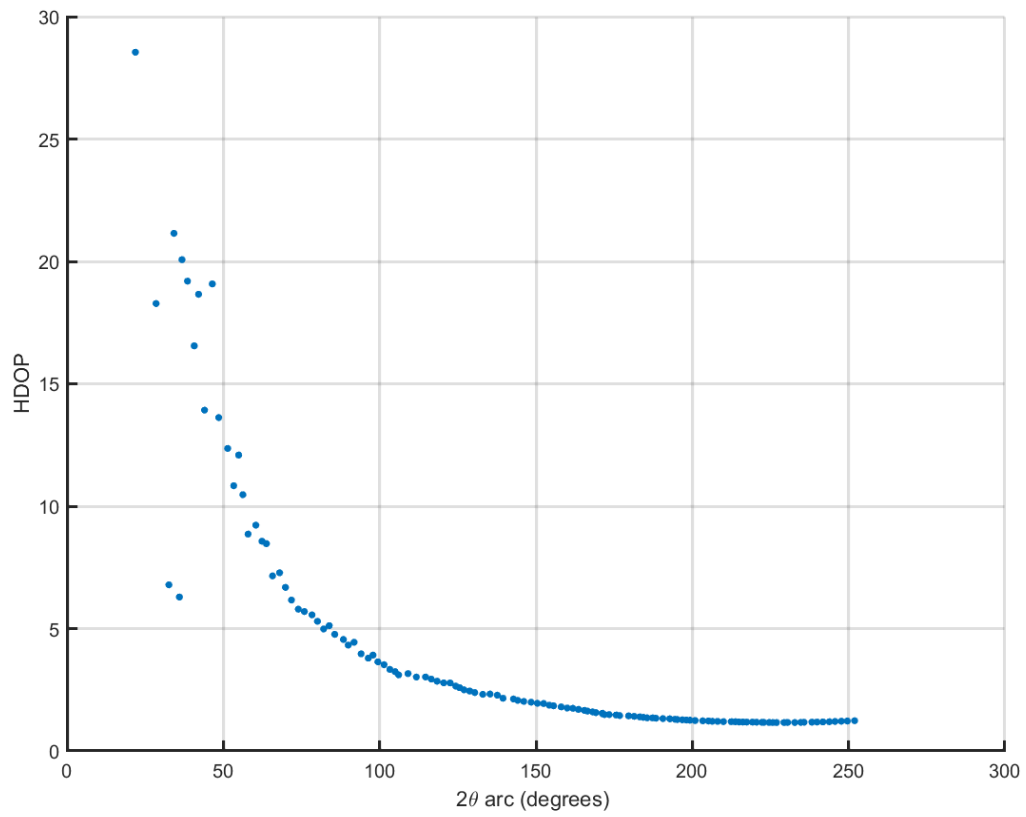
Figure 2.6. Data results for evenly spaced survey points with increasing arc 2θ

fully maximize the precision, a survey arc of about 200° should be driven around the transponder. After 200°, the HDOP value does not significantly improve as arc length increases.

2.3.2 Monte Carlo Selection

A Monte Carlo study was also formulated to assess the impact of random sampling on the survey perimeter to the localization solution. Three random points around the survey were chosen to assess the resultant least-squares solutions' accuracy and precision. Here, the survey points chosen do not have to be evenly spaced by θ degrees, nor does the first point chosen reside at the first survey point taken in the data set. A total of 100,000 different three-point combinations were tested to determine the geometric locations of the three survey points yielding the lowest error when compared to the ground truth position. Fig. 2.7 shows a trend that the lowest error values occur at larger arc lengths and the largest errors are found near the origin of the graph. It is interesting to note that the graph is symmetric around the line $\theta_1 = \theta_2$, even though the radius does not completely remain constant in this data set. There is also a distinct trend of reduced error above the line $\theta_1 + \theta_2 = 150°$, shown as the magenta line in Figure 2.7. Thus, an ASV must drive at least a 150° arc to yield an error of less than 2 meters. Further tests could determine how sensitive the error is to the magnitude of the radius of the circle, or the distance between the ASV and the transponder.

2.4 Least-Squares Solution on Aug. 2023 Data Set

The same least-squares algorithm was then run on the L-shaped survey. As seen in Figure 2.8, the least-squares method predicts a location about 70 m west and 10 m south of the drop location. While the drop location is not meant to be considered the "true" location of the
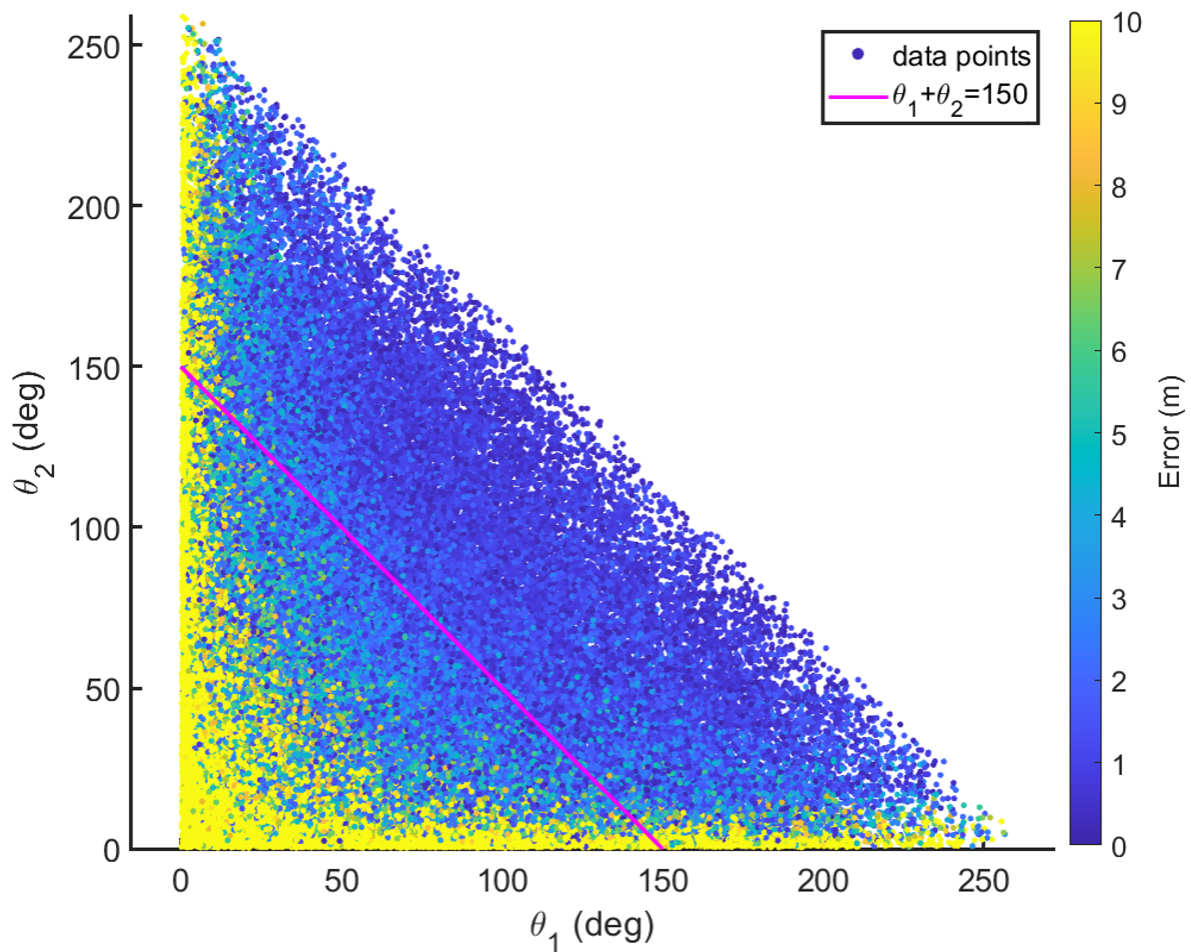
Figure 2.7. Results of 100,000 Monte Carlo choices of 3 points around the survey at random. The color variable illustrates how close each solution is to the ground truth of this study. A proposed trend line for low-error solutions is shown in magenta.
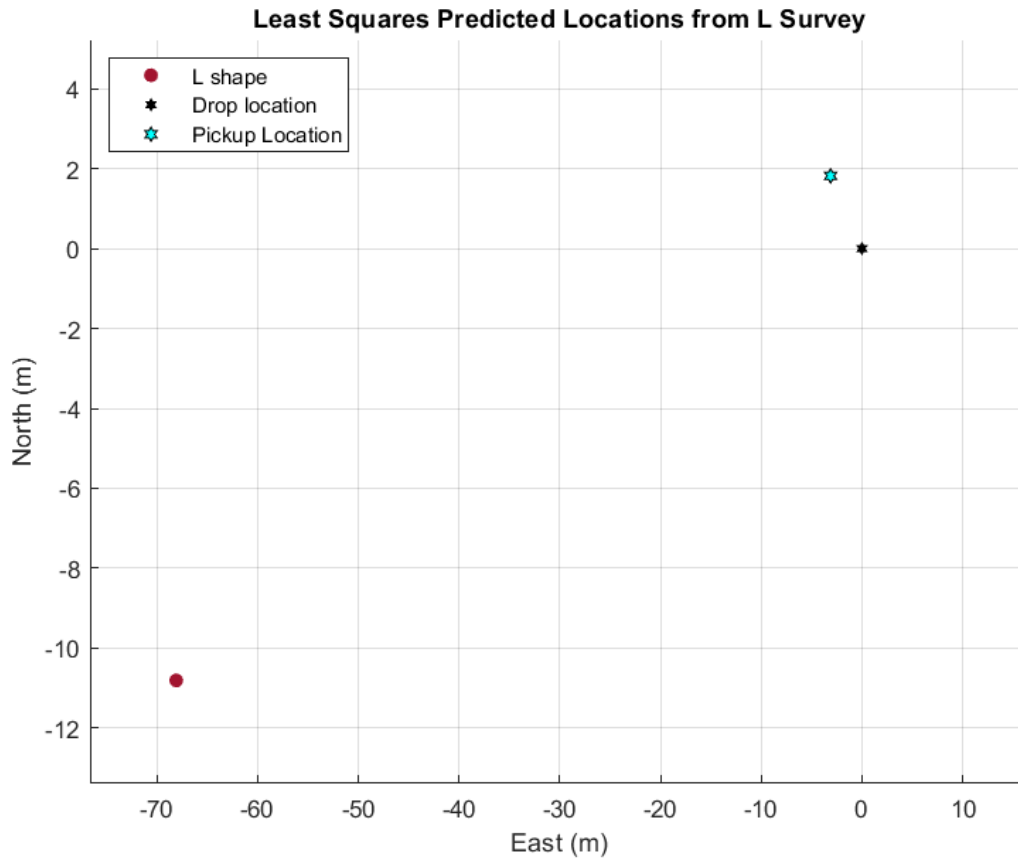
Figure 2.8. Least-squares solution results for the August L-shaped survey

transponder, it does seem far-fetched that the transponder would move over 70 m while dropping

30 m to the seafloor. It is highly likely that the noisy data seen in Section 1.4.2 is one cause

of this westward bias. This result indicates that a filtering algorithm is needed to predict more

accurately the transponder location for navigation missions.

2.5 Conclusions on the Least-Squares Method

Dilution of precision analysis yields insightful information about the required measure-

ment spacing around the survey arc. From both the theory and the evenly spaced θ arc length

study, a high-precision survey would require an arc length between $150°$ to $250°$ around the

transponder. An arc length in this range would lead to a reduced error ellipse surrounding the estimated transponder location. This same arc length is necessary to resolve an accuracy of less than 2 meters. This result indicates that traveling close to a semi-circle around the transponder achieves sufficient precision. Traveling the remaining half of the survey circle does not yield any significant improvement to the transponder location estimate.

The least-squares solution described herein does not consider all potential sources of uncertainty. The ultimate goal of this application is to estimate the position location of the transponder to within two to three meters of accuracy in any direction. Thus, the rest of this paper includes implementing an Extended Kalman Filter (EKF) to perform ongoing localization and error estimates while an ASV performs the survey arc. The EKF formulation will include both distance measurement uncertainty as well as uncertainty in the ASV position. An embedded implementation is envisioned which will guide behavior of the ASV and allow it to end its survey when the transponder position error meets a set threshold.

Chapter 2, in part, is a reprint of the material as it appears in Sawyer, L., Anderson, M., Bednar, R., Merrifield, S., and Terrill, E., "Seabed Transponder Localization Behavior from an Autonomous Surface Vehicle," OCEANS 2023 - MTS/IEEE U.S. Gulf Coast, Biloxi, MS, USA, 2023. pp.1-7. The thesis author was the primary investigator and author of this paper.

Chapter 3

Kalman Filter Development

3.1   Kalman Filter Development

The least-squares method is unable to adequately address all sources of uncertainty in this application. There is also little agreement between the predicted solution and expected location of the transponder from the August 2023 experiment, with the predicted position varying by over 70 meters from the drop location in Fig. 2.8. The Kalman filter was chosen because of its ability to provide an assessment of the uncertainty of the estimate, as well as its ability to perform a gating routine for acoustic responses that are considered outliers.

An extended Kalman filter was implemented because the range equation, Eq. (2.3) is nonlinear with respect to transponder position. The two measurements it processes (GPS and acoustic pseudorange) are received on different timescales; the GPS measurement is taken at 1 Hz, and the acoustic pseudorange is available at 0.1 Hz. Each individual measurement has its own processing subroutine that updates the entire state vector and state covariance matrix after the measurement is processed. Finally, the last subroutine included in the algorithm is a gating function that separates and rejects a distorted or noisy measurement from likely data points using the statistics of previous measurements. As seen in the data from the August 2023 experiment,

Table 3.1. Kalman Filter State Variables and Matrix Definitions

Matrix Name	Variable	Size of Matrix
State Vector	x	6x1
State Transition Model	ϕ	6x6
State Covariance Matrix	P	6x6
Process Noise Covariance	Q	4x4
Noise Distribution Matrix	G	6x4
Transponder Observation Model	H_t	1x4
Transponder Observation Noise Covariance	R_t	1x1
Sub Observation Model	H_s	4x6
Sub Position Noise Covariance	R_s	4x4

there were many extraneous data points that were likely the result of false detections by the acoustic transducer.

Because the Kalman filter is a well-known tool used in guidance, navigation, and control, the derivation of the mathematics will not be explicitly shown in this paper. However, the specific equations and parameters that are used for this algorithm will be denoted, as well as the nomenclature used for the variables and the dimensions of each of the matrices [21]. These will be explained further in the next section.

3.2   Kalman Filter Parameters

The state vector for this application is a 6x1 vector, which includes the east and north coordinates of the transponder, the east and north components of the ASV sub position, and the east and north velocities of the sub. Table 3.1 lists each variable, its dimension, and its definition.

The prediction for the state vector x is updated at each time step dt. The value of dt changes depending on how much time has elapsed since a previous measurement was received and

processed; typically, dt is one second since this is the elapsed time between GPS measurements.

The values for the block diagonal process noise covariance matrix (Q) were chosen as follows: The first two entries represent that there should only be minimal movement of the transponder in the east and north directions. The final two entries were chosen to represent the maximum speed of the ASV, 0.5 m/s, in the east and north directions. The time constant, τ, in the state transition matrix ϕ, is set to 40 seconds. The prediction of the state is calculated in Eqs. (3.1) and (3.2), where x and P are defined below.

$$\hat{x}_k = \phi x_{k-1} \tag{3.1}$$

$$\hat{P}_k = \phi P_{k-1}\phi^T + GQG^T \tag{3.2}$$

$$x = \begin{bmatrix} x_t \\ y_t \\ x_s \\ y_s \\ u_s \\ v_s \end{bmatrix}, \ \phi = \begin{bmatrix} 1 & 0 & 0 & 0 & 0 & 0 \\ 0 & 1 & 0 & 0 & 0 & 0 \\ 0 & 0 & 1 & 0 & dt & 0 \\ 0 & 0 & 0 & 1 & 0 & dt \\ 0 & 0 & 0 & 0 & 1-\frac{dt}{\tau} & 0 \\ 0 & 0 & 0 & 0 & 0 & 1-\frac{dt}{\tau} \end{bmatrix}$$

$$Q = \begin{bmatrix} 0.01 & 0 & 0 & 0 \\ 0 & 0.01 & 0 & 0 \\ 0 & 0 & 0.25 & 0 \\ 0 & 0 & 0 & 0.25 \end{bmatrix}, \; G = \begin{bmatrix} dt & 0 & 0 & 0 \\ 0 & dt & 0 & 0 \\ 0 & 0 & 0 & 0 \\ 0 & 0 & 0 & 0 \\ 0 & 0 & \frac{dt}{\tau} & 0 \\ 0 & 0 & 0 & \frac{dt}{\tau} \end{bmatrix}$$

Mean state and covariance predictions for each time step k are denoted by the hat symbol, seen as $\hat{x}$ and $\hat{P}$. Once a measurement is received, the innovations covariance matrix S and the Kalman gain K are computed via Eqs. (3.3) and (3.4).

$$S = H\hat{P}_k H^T + R \tag{3.3}$$

$$K = \hat{P}_k H^T S^{-1} \tag{3.4}$$

The observation model H and the observation noise covariance R depend on the type of measurement received at each time step. These will be described for each individual measurement in sections 3.2.1 and 3.2.2.

Once the Kalman gain is calculated, the state vector and state covariance matrix are updated for the next state estimate, as shown in Eqs. (3.5) and (3.6).

$$x_{k+1} = \hat{x}_k + K(z_k - H\hat{x}_k) \tag{3.5}$$

$$P_{k+1} = (I - KH)\hat{P}_k \tag{3.6}$$

37

The vector z_k represents the measurement vector received at time k, and I denotes the

identity matrix. In this case, I is 6x6 to match the size of P.

3.2.1 Transponder Measurements

The state vector includes estimates of the east and north components of the transponder

location. As mentioned in Section 2.1.1,these variables are expressed in a Cartesian plane with

the origin taken as the drop location of the transponder. The covariance matrix of observation

noise, R, represents the inherent sensor accuracy and processing time of the acoustic modem,

and its dimension is 1x1. The state transition matrix, ϕ, assumes that the transponder remains

nearly stationary once it lands on the seafloor.

The observation model matrix used in the transponder measurement subroutine is that of

an "extended" Kalman filter because the range equation is nonlinear. Its size is a 1x6 matrix, and

it uses the partial derivative of the range equation with respect to each variable that it multiplies

with in the state vector. The composition of the observation model matrix, H, is revealed in Eq.

(3.7).

$$H_t = \begin{bmatrix} \frac{\delta r}{\delta x_t} & \frac{\delta r}{\delta y_t} & \frac{\delta r}{\delta x_s} & \frac{\delta r}{\delta y_s} & 0 & 0 \end{bmatrix} = \begin{bmatrix} \frac{x_t - x_s}{r} & \frac{x_s - x_t}{r} & \frac{y_t - y_s}{r} & \frac{y_s - y_t}{r} & 0 & 0 \end{bmatrix} \qquad (3.7)$$

where r is the distance from the sub to the transponder:

$$r = \sqrt{(x_S - x_t)^2 + (y_s - y_t)^2)}$$

Table 3.2. Standard deviation of sensors used in Kalman filter measurements.

Variable	Standard Deviation	Value
σ_t	Transponder	0.0002 s
σ_{fl_E}	GPS East Position (on float)	2.07 m
σ_{fl_N}	GPS North Position (on float)	2.08 m
σ_{v_E}	GPS East Velocity	0.06 m/s
σ_{v_N}	GPS North Velocity	0.06 m/s
σ_b	Horizontal Tether Offset	2 m
σ_{owtt}	Pseudorange Measurement	**Dec:** 14 m **Aug:** 255 m

The observation noise covariance matrix is a single value that incorporates the variance of the transducer time estimate and the variance of the pseudorange measurements, as seen in Eq. (3.8). The December survey, since it had fewer outliers, has a smaller observation noise covariance value when compared to the August 2023 data. The full values for each of the sensor standard deviations can be found in Table 3.2.

$$R_t = (\sigma_t * c)^2 + \sigma_{owtt}^2 \tag{3.8}$$

3.2.2 Wave Glider Measurements

The Kalman filter also predicts the location and velocity of the ASV; specifically, this algorithm predicts these states for Wave Glider sub component using the GPS data. The GPS receiver is located on the float of the Wave Glider, but the acoustic measurements are being received from the sub. As seen in Fig. 1.5, the sub is attached to the float by an 8.5 meter tether that is free to oscillate, much like a pendulum, as the Wave Glider travels forward. In order to account for this distance, the model introduces an average distance the sub sits in front of the float, as well as a standard deviation of the sub position. The sub's movement is assumed to
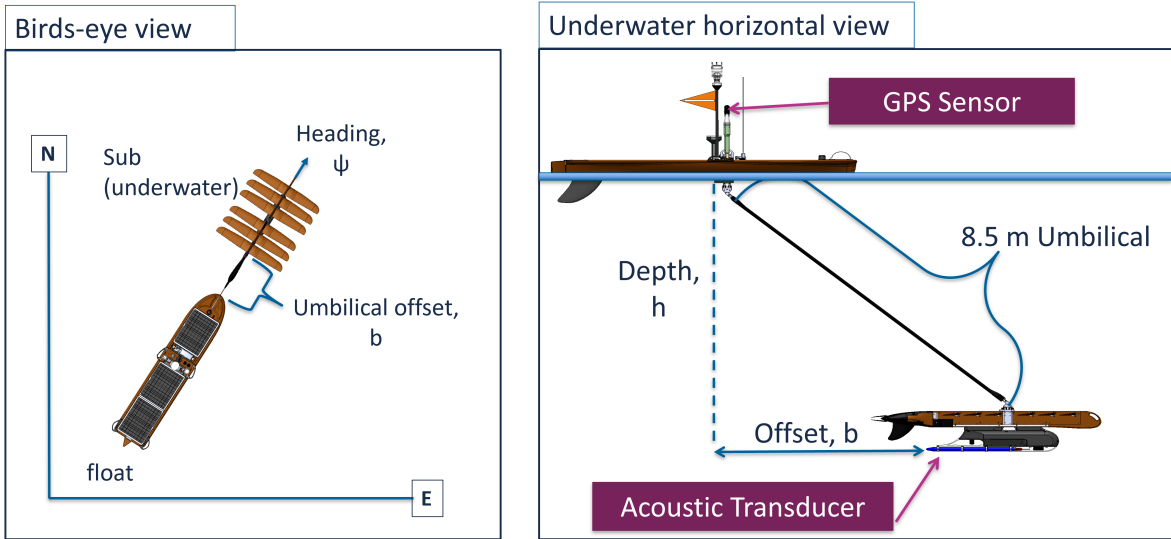
Figure 3.1. Left: Bird's eye view of Wave Glider with extended sub component. Right: Plane view of the surface float and underwater sub component offset. The hypotenuse length is 8.5 m

be constrained by two factors: it does not oscillate out of the forward plane of motion of the float, and it is nearly always in front of the float to drive the float's motion. Thus, in Fig. 3.1, it can be seen that the model will keep the heading of the sub the same as the vehicle's heading as reported by GPS. The offset (b) of the sub from the float will be modeled in (3.9) below:

$$b = \bar{b} + \varepsilon_b \tag{3.9}$$

where the mean offset ($\bar{b}$) is assumed to be 2 m and ε_b is assumed to be zero-mean Gaussian with a standard deviation of σ_b.

The mean offset of 2 meters is chosen to reflect the low sea state during both experiments. If the significant wave heights were larger, then a new motion model would be needed to account for more vertical oscillations in the Wave Glider's movement. Further, this model is constrained

to smaller sea states because there is little pitch and roll movement affecting the GPS sensor's displacement from the center of the body of the Wave Glider.

The GPS receiver can also estimate the velocity of the ASV, and then that velocity is split into its x and y components using the reported heading (ψ) of the ASV. Thus, the state vector is composed of positions x and y, as well as velocities u and v (all within the Cartesian plane). The observation model matrix is given in (3.10).

$$H = \begin{bmatrix} 0 & 0 & 1 & 0 & 0 & 0 \\ 0 & 0 & 0 & 1 & 0 & 0 \\ 0 & 0 & 0 & 0 & 1 & 0 \\ 0 & 0 & 0 & 0 & 0 & 1 \end{bmatrix} \tag{3.10}$$

The observation noise covariance matrix, R, reflects the uncertainty parameters of the GPS in meters (for x and y) and meters per second (for u and v), which can be found in Table 3.2. Because the standard deviation of the sub must be accounted for, the observation noise covariance matrix is a 4x4 matrix composed as seen in Eq. (3.11) with a heading angle (ψ) obtained from GPS.

$$R_s = \begin{bmatrix} R_x & & 0_{2x2} \\ \hline & \sigma_{v_E}^2 & 0 \\ 0_{2x2} & & \\ & 0 & \sigma_{v_N}^2 \end{bmatrix} \tag{3.11}$$

where

$$R_x = \begin{bmatrix} \sigma_{fl_E}^2 & 0 \\ 0 & \sigma_{fl_N}^2 \end{bmatrix} + \sigma_b^2 \begin{bmatrix} sin^2\psi & sin\psi\,cos\psi \\ sin\psi\,cos\psi & cos^2\psi \end{bmatrix}$$

3.3   Setup and Timing

The duty cycle is such that a GPS measurement is received once every second, or 1 Hz, and a range measurement is received every 10 seconds, or 0.1 Hz. The GPS measurements are received more frequently than the range measurements, so the two observation updates must run on different timescales. This is accomplished by reading in the timestamp of each new measurement, then computing the elapsed time between the previous timestamp and the most recent one. The GPS subroutine updates its position estimate at each timestamp, regardless of which measurement has been taken. However, the range and transponder location update will only occur when a range measurement is received. This allows the algorithm to continuously run, even when a measurement is not received or processed properly. It also allows the gating function to determine whether a range measurement will be processed or not. If the measurement passes the validation gate, the timestamp is recorded and the motion update will occur; otherwise, the measurement is discarded and the next measurement received will drive the motion update.

The validation gate is governed by Eq. (3.12) and provides a statistical estimate of how large the next range measurement should be [21] [22]. It is governed by the innovations covariance matrix from Eq. (3.3) and the measurement error residuals calculated during each update step [22]. If the product of Eq. (3.12) is below a set threshold that is proportional to σ_{owtt}, then the measurement will pass the validation gate and the measurement will be processed,

as well as an estimate update. If it does not pass the validation gate, the measurement will be discarded, and the algorithm will wait for the next measurement update. The validation gate is only implemented for range measurements because the GPS measurements are much more reliable and are not subjected to environmental conditions like false detections and acoustic multipath effects.

$$g^2 \geq y_k \, S_k^{-1} \, y_k' \tag{3.12}$$

$$g^2 = \frac{(20 \, m)}{\sigma_{owtt}}$$

3.4 Algorithm Validation

A simulation was created to validate the Kalman filter algorithm and to assess the performance of the final transponder location prediction method. A validation data set is also created by setting a constant velocity and radius of the survey circle. The ASV starts with a heading of 0 degrees, and its starting location is arbitrary. While the position units are in meters for the simulation, all the coordinates are set in the Cartesian plane to avoid errors when converting between geodetic coordinates and Cartesian coordinates. The length of the time series is also determined at the beginning of the simulation, which will determine how far around the circle the ASV will travel. The constant velocity, V, and radius, ρ were chosen at the beginning. To match the December survey parameters, V and ρ were set to 0.5 m/s and 150 m, respectively.

After the initial parameters are selected, the time rate of change of the heading for the ASV during the simulation is determined by the equation of the circumference of a circle. Since the velocity magnitude and radius are known, it can be determined how fast the ASV changes its heading over the course of the full circle in Eq. (3.13), yielding a heading measurement for

every time step.

$$2\pi r = V\Delta t = V\frac{360°}{\dot{\theta}} \implies \dot{\theta} = \frac{V * 180°}{\pi\rho} \tag{3.13}$$

Where $\dot{\theta}$ is given in degrees per second. The u and v measurements are determined by multiplying the sine and cosine of the heading (respectively) by the velocity magnitude.

To introduce some noise into the simulation data, each data vector is corrupted by the uncertainty of each sensor (given in Table 3.2) using a randomly generated Gaussian white noise signal. This process allows the dataset to have significant variance, as well as some data points that may not pass the validation gate. Once the pseudorange data was created with added noise, five of the measurements were selected at random and multiplied by 10 to introduce outliers in the data set. This was done to test how the validation gate would react to poor data measurements. The simulation data is then processed by the Kalman filter algorithm, and the results can be seen in the figures below.

The simulated transponder location was located at 300 meters due east of the origin. The result of the Kalman Filter model depicts an estimated location seen in Figure 3.4, which yields a transponder estimate that is only 35 centimeters away from the known truth of this simulation. The validation simulation also ensures that the sub velocity is being estimated accurately, as demonstrated in Figures 3.2 and 3.3.

It can be seen in Figure 3.5 that the area of the transponder position covariance ellipse reaches a steady state once the ASV in the simulation has traveled approximately 150 degrees. The orientation of the ellipse will continue to change with the orientation between the ASV and the transponder, but the major and minor axes of the covariance ellipse will remain the same.
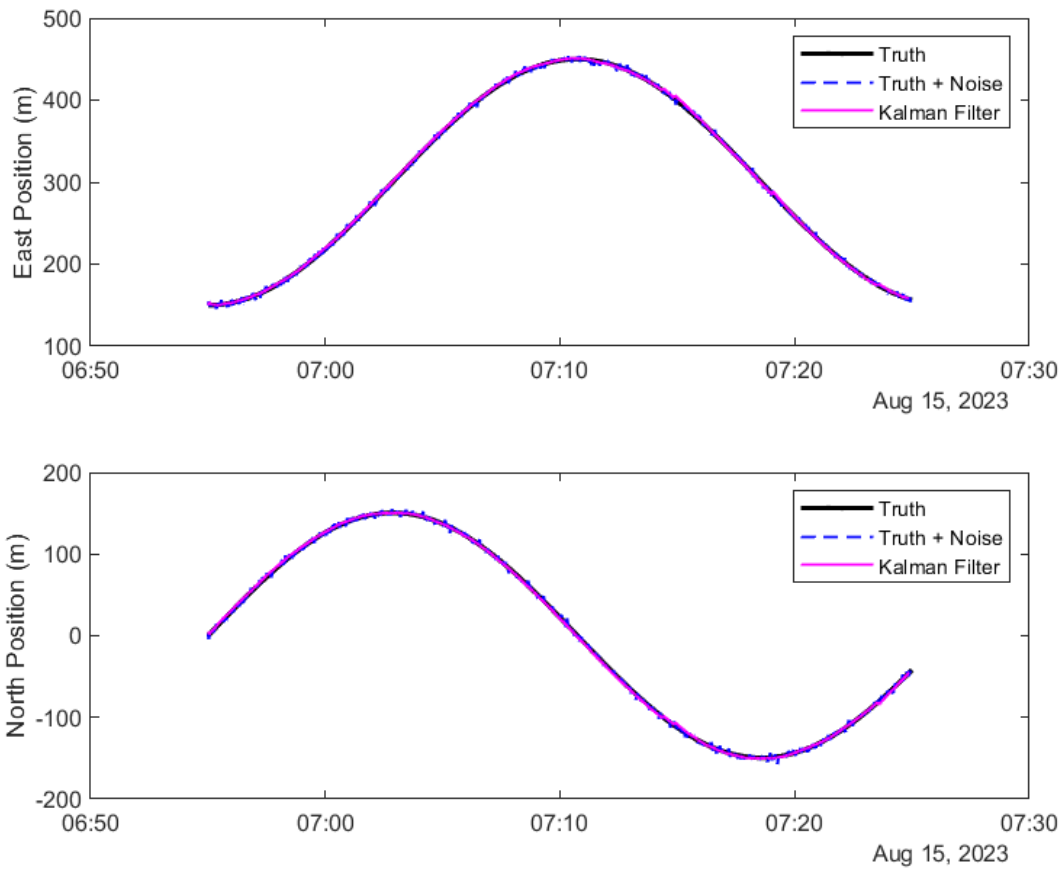
44

Figure 3.2. Kalman Filter simulation position results. Top: x or east direction path. Bottom: y or north direction path.
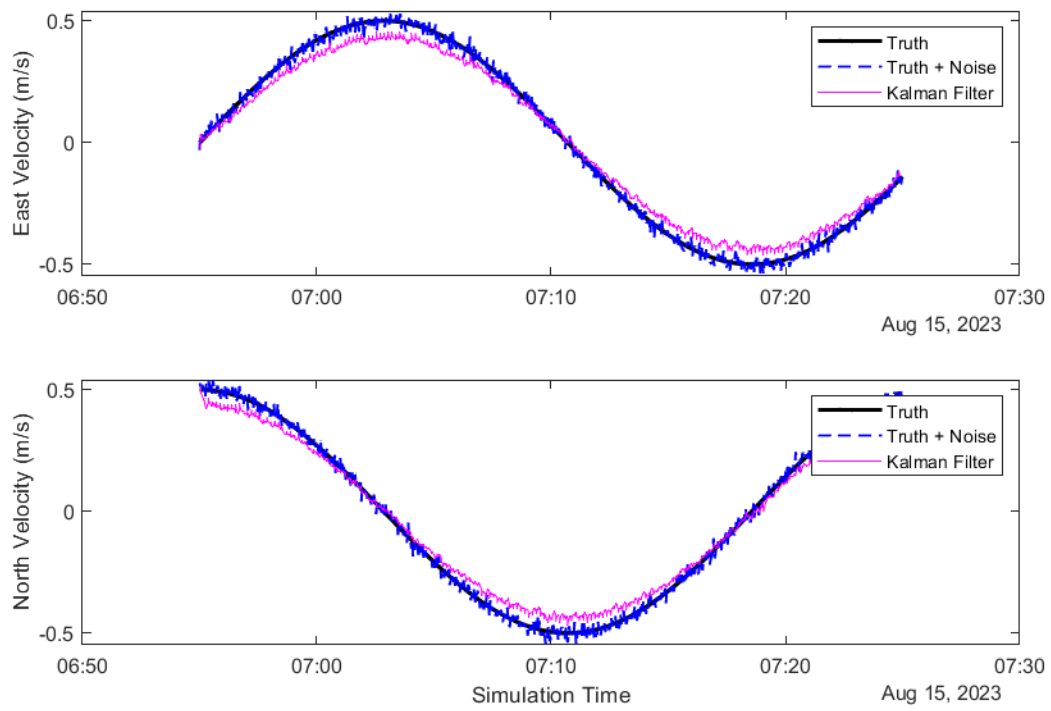
Figure 3.3. Kalman Filter simulation velocity results. Top: u or east velocity estimate. Bottom: v or north velocity estimate.
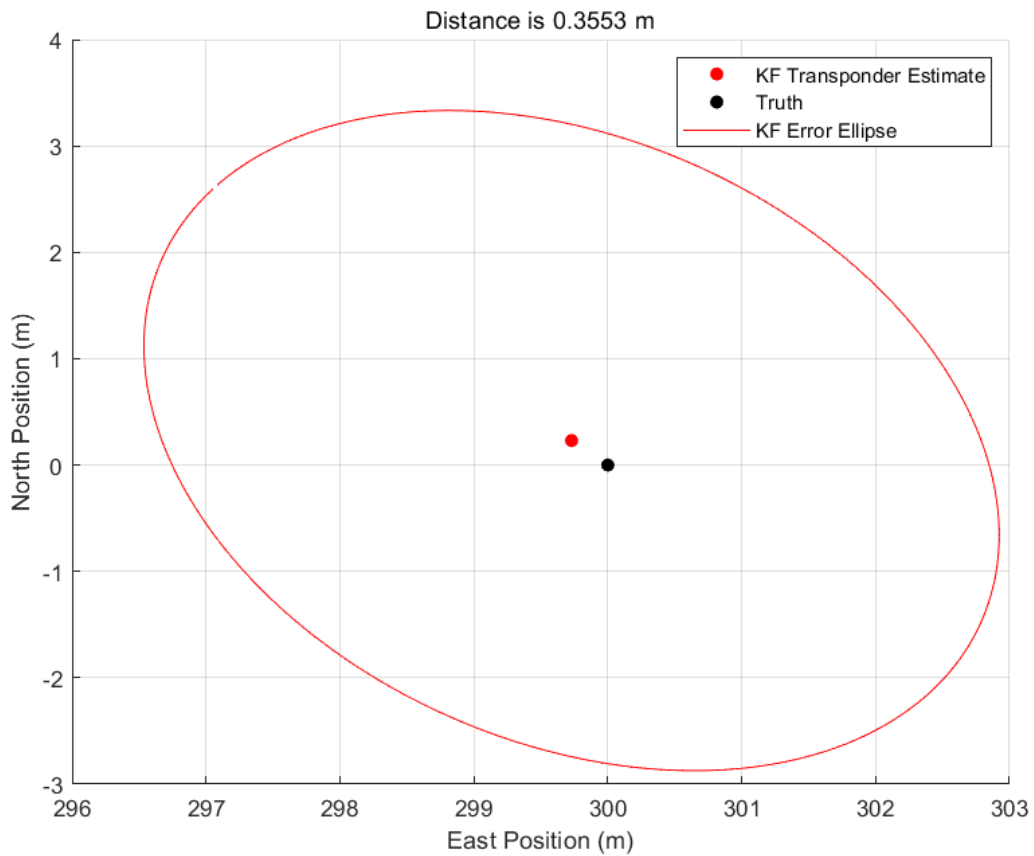
Figure 3.4. Final estimate of the simulated transponder location. The chosen location for the truth value is shown in black. The position error covariance ellipse is also shown for reference. The final distance between the Kalman Filter's estimate and the true location is 35 centimeters.
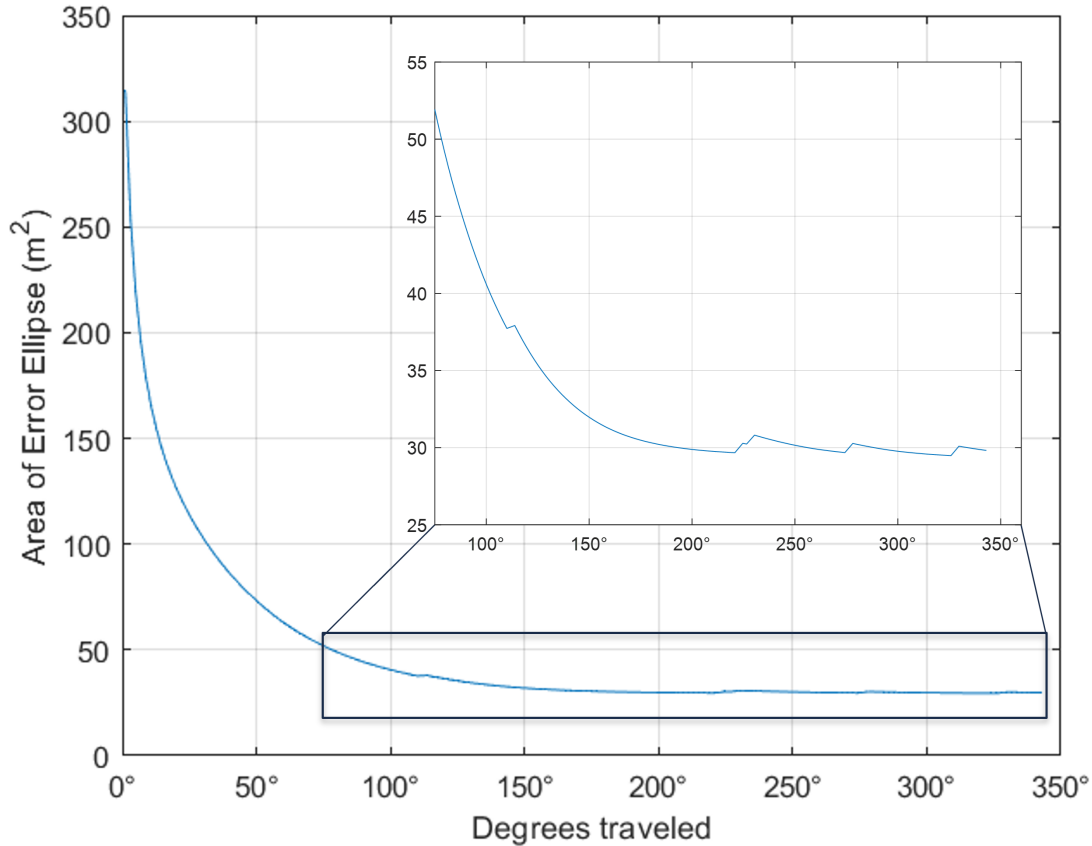
Figure 3.5. Convergence of covariance error ellipse by arc length traveled around the circle. Zoom in shows final area of error ellipse and spikes in covariance matrix from missed validation gate measurements.

This result further validates the theoretical assessment from Section 2.2.1.

The spikes seen in Figure 3.5 are due to the five outlier measurements that were included in the simulation data. These results demonstrate that the validation gate is functioning properly, and that the estimate is able to recover after a measurement is missed. It is to be expected that after a missed measurement the covariance ellipse will grow, but the fact that the precision and covariance ellipse are able to recover to the steady-state values demonstrates that datasets with outliers can still provide accurate assessments to the final transponder location.

Chapter 4

Kalman Filter Results and Analysis

4.1 Results of Kalman Filter Location Estimates

The Kalman filter was run on both of the data sets to determine an estimate of the transponder location for each experiment. In the August experiment, the pickup location of the transponder was also recorded at the end of the testing week. This gives a better idea of where the true location of the transponder could have been during the week of testing. The pickup location that was recorded was approximately 3 meters away from the drop location, which implies that the transponder did not move more than within a 5 meter radius of the drop location as it was settling to the seafloor.

The relationship between arc length traveled around the survey circle and the accuracy of the estimate is further explored in the December Kalman filter results. This data set will be discussed first, and then the idea of driving straight-line transects instead of arcs will be explored through the results of the August L-shaped survey. The L-shape serves to analyze how the estimate and the covariance ellipse changes after just one leg of the survey (traveling the equivalent of 90 degrees if it were a circular arc) versus traveling both legs (equivalent to a 180 degree arc). According to the theory presented in Chapter 2, traversing both of the legs of the

L-shape should be sufficient to provide a precise estimate of the transponder location.

4.1.1 December 2022 Circular Survey Results

The results from the Kalman filter analysis suggest that the transponder is located approximately 10 meters east and 7 meters north of the drop location recorded when the experiment began (see Figs. 4.1 and 4.2). The covariance ellipse generated with the final estimate encompasses an area of approximately 25 meters squared after the covariance ellipse converges. It is clear from the convergence graph that, after traveling 150 degrees around the circle, the area of the covariance ellipse only continues to decrease by another 5 to 10 meters squared. This result agrees with the theory shown in Chapter 2 and the simulation results seen in Chapter 3. After traveling 200 degrees around the circle, the covariance ellipse ceases changing its area and stabilizes at the constant 25 meters squared, shown in Fig. 4.3. It can be concluded that, to maximize the precision of the transponder estimate, only 150 or 200 degrees of the survey arc needs to be traversed.

4.1.2 August 2023 L-shape Survey Results

The L-shape survey data has much more noise than the December circular survey data set. This can be seen when comparing Figs. 1.4 and 1.6, where it is evident that the pseudoranges do not have many outliers in the December data. The L-shape survey has outliers that appear far away from the estimated distance of the ASV to the transponder. The probability density functions in Figure 4.4 show that while the majority of the transponder pseudorange data aligns with the ASV's physical distance from the drop location, there is an elongated tail at either end of the distribution. Because the Kalman filter assumes Gaussian distributed data, this can lead to
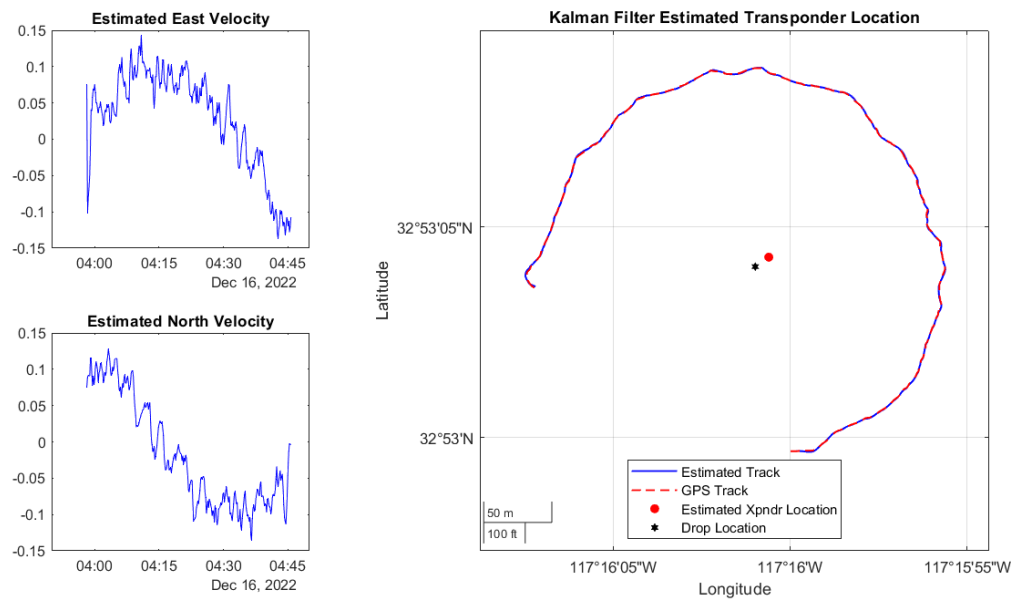
Figure 4.1. Results of the Kalman filter applied to the December 2022 circular survey.

a source of error for the Kalman filter. However, with the implementation of the validation gate, it is seen that after the Kalman filter is run, the processed pseudorange data both better aligns with the expected distance from the transponder, and the tails of the dataset are eliminated. Thus, the Kalman filter is able to process the dataset without this inherent source of error. This proves that the algorithm presented in this paper is robust enough to handle noisy datasets and outliers without affecting the overall accuracy of the position estimate.

The results from the L-shape survey suggest that the transponder may have shifted east 5 meters and north 1 meter as it was settling to the seafloor. Based on the added information of recording the pickup location for this experiment, this seems like a feasible solution for the true transponder location. The covariance ellipse is much larger than the ellipse seen in the December dataset due to the larger range of the survey (1.5 km versus 150 meters), but it encompasses an approximate area of 750 meters squared (seen in Figure 4.5). The small jumps in the area that
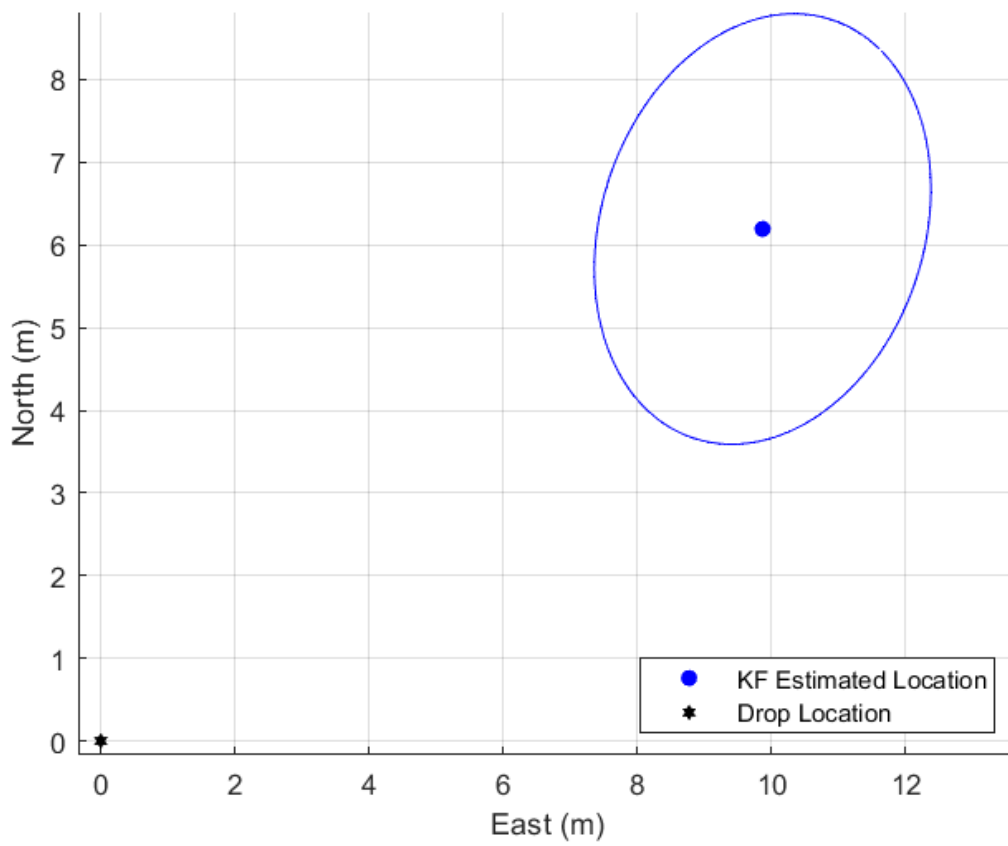
Figure 4.2. Covariance error ellipse defining the area of uncertainty around the final transponder estimate for December 2022.
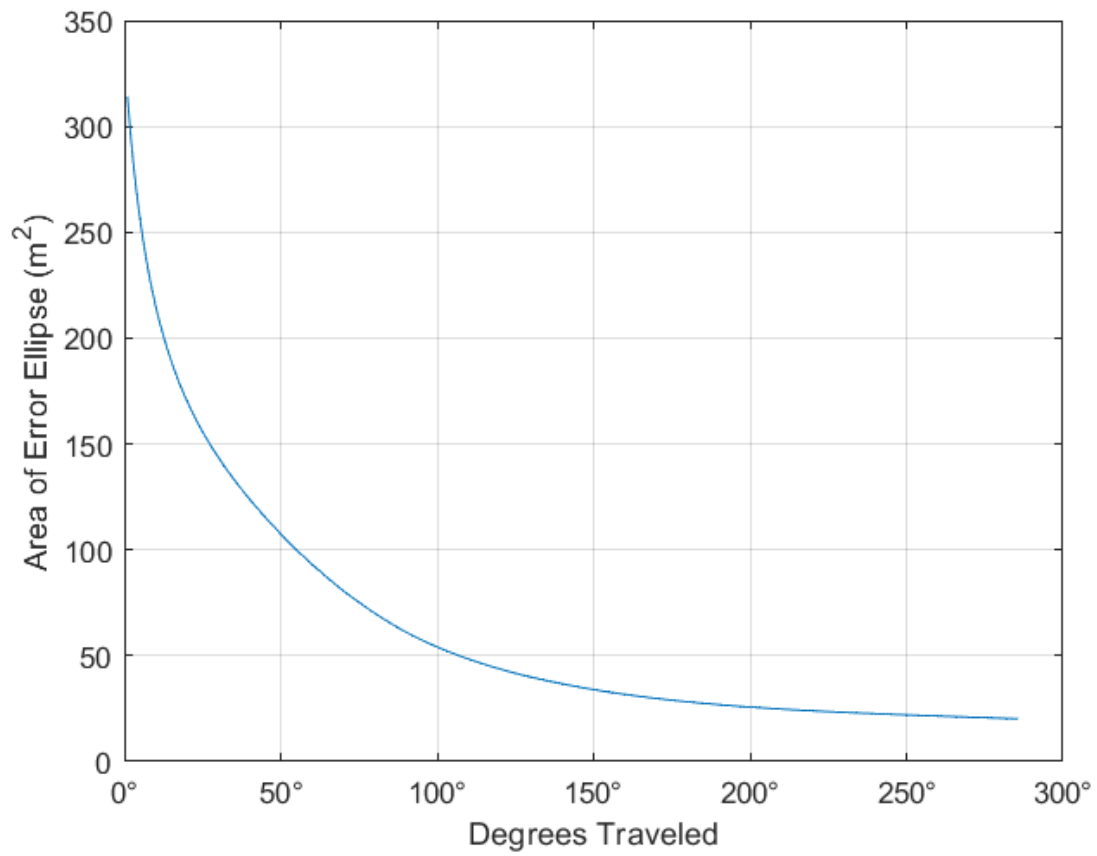
Figure 4.3. Convergence of the area of the covariance error ellipse in the December 2022 survey.
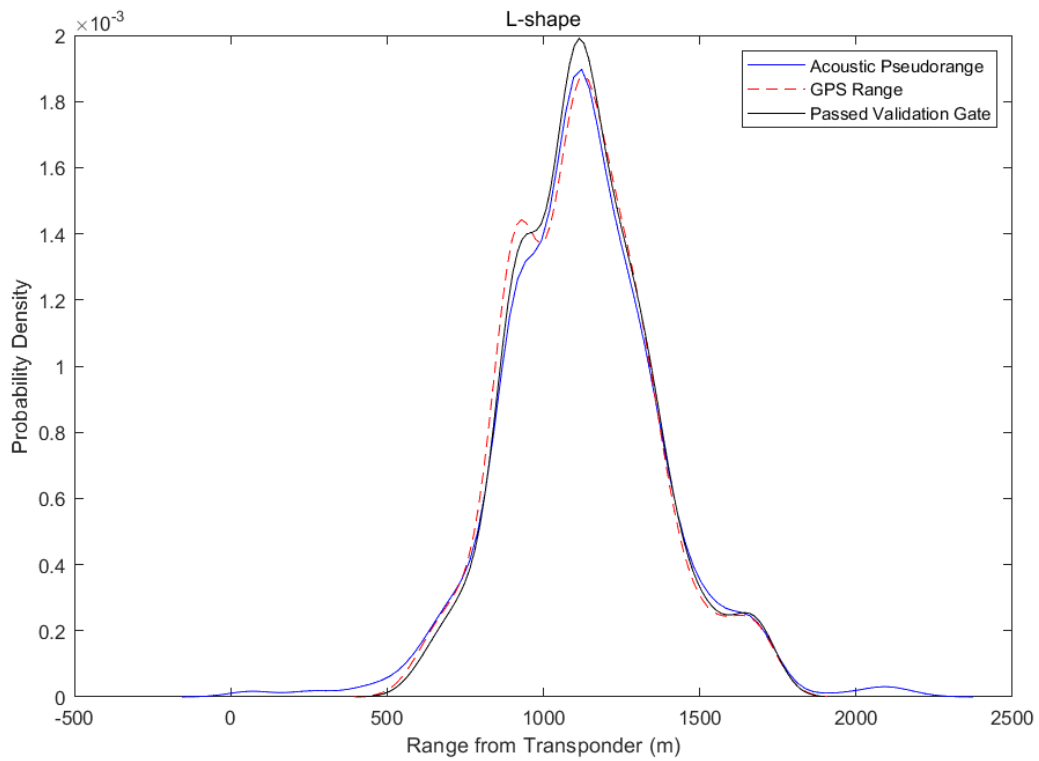
Figure 4.4. Probability density of the pseudorange measurements as well as the distance from the ASV to the drop location. Also pictured is the probability density of the pseudoranges of only the data points that passed the validation gate within the Kalman filter.
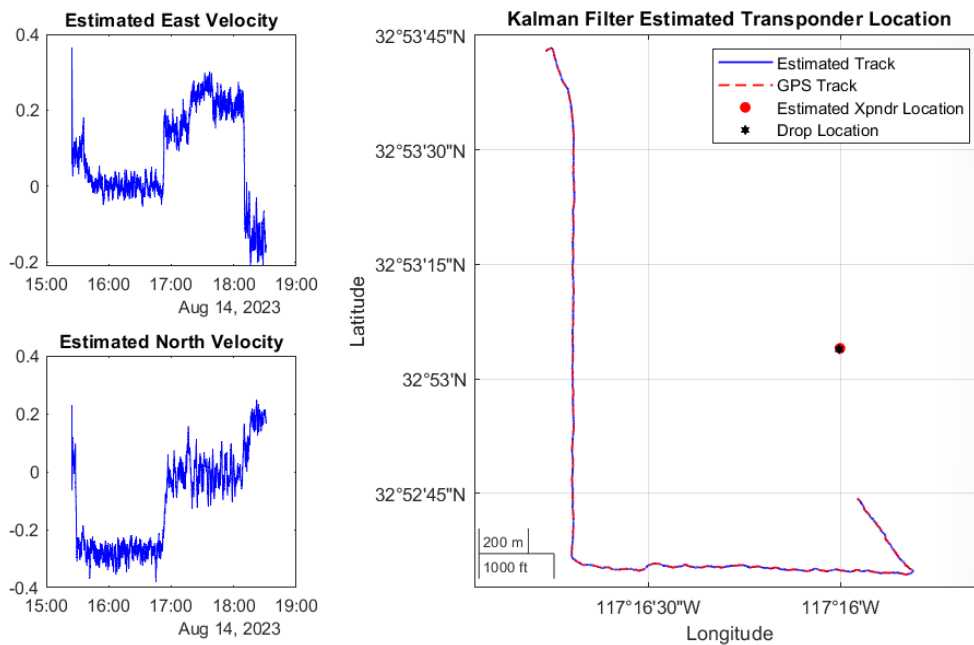
Figure 4.5. Results of the Kalman filter from the August 2023 L-shape survey

can be seen throughout the survey are due to the missed validation gate of some measurements. It is clear that the filter will recover quickly after a missed measurement, without too much effect on the overall position estimate and precision. Further investigation is needed to investigate the effect of the radius of the survey versus the final covariance error ellipse area encompassed.

It was also worthwhile to see how the estimate changed from the L-shaped survey if only part of the survey was completed. The two legs of the L-shape provide a 90 degree and 180 degree (respectively for each leg) estimate of a square inscribed into a circle.

The error ellipse shrinks as more distance is covered in Fig. 4.7. From Fig. 4.6, it can be seen that convergence of the covariance ellipse is only reached towards the end of the survey. The 90 degree heading change occurs at a distance of 2 kilometers. This result is consistent with the previous data suggesting that convergence is reached at 150 degrees. Further, it seems that the area of the error ellipse halves between the first and the second leg of the survey, indicating
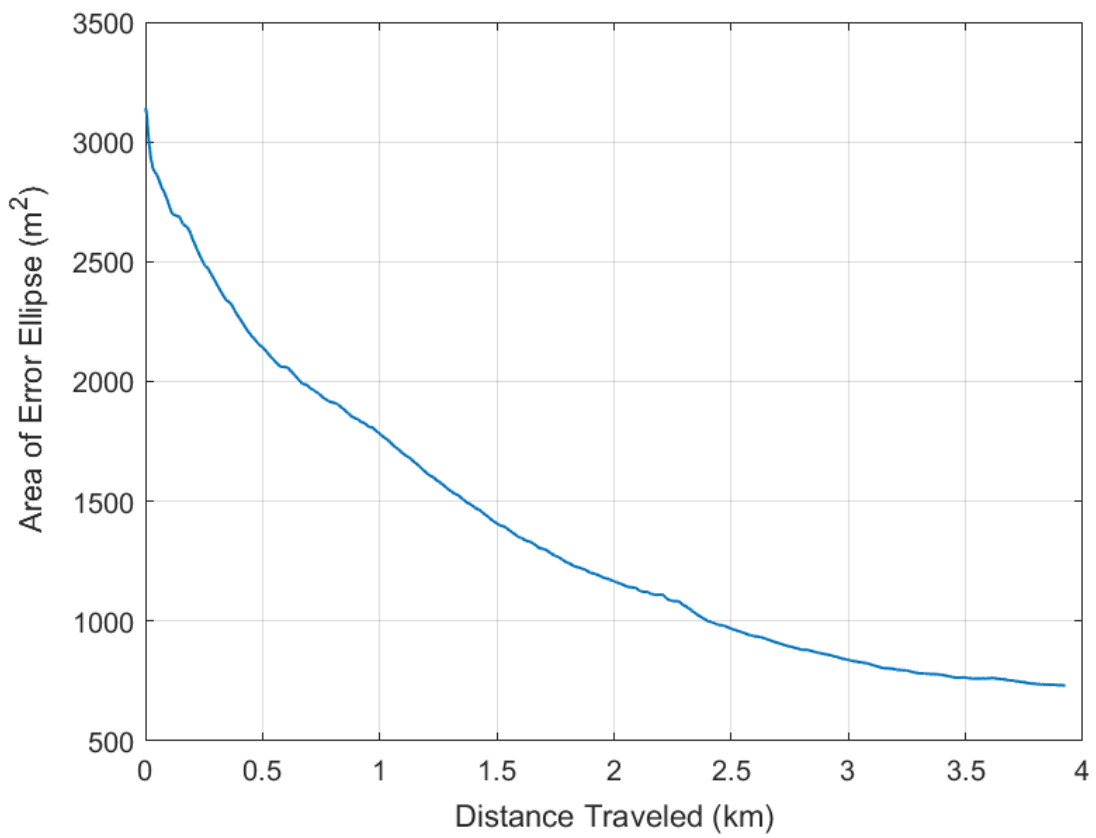
55

Figure 4.6. Convergence of the area of the covariance error ellipse for the August 2023 L-shape survey
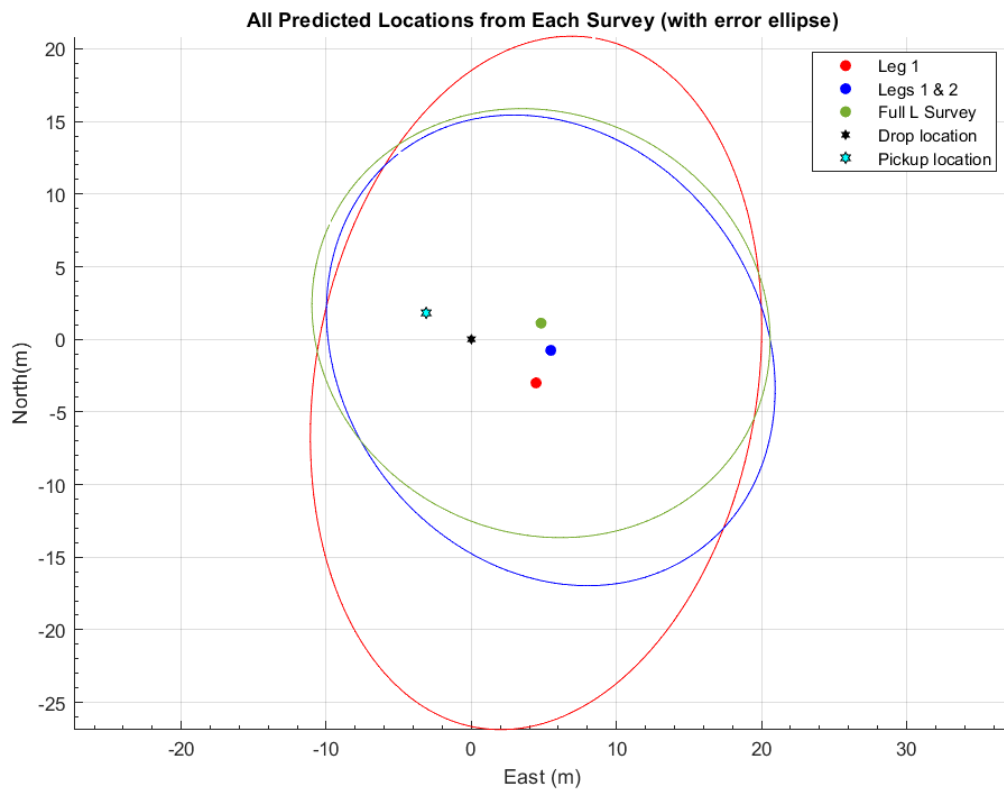
Figure 4.7. Transponder position estimates for the full L-shape survey, one leg, and two legs respectively.

that it is imperative to perform over 90 degrees equivalent of a circular survey arc.

4.2   Final Analysis

From these results, it can also be concluded that traveling an arc of no more than 200 degrees yields a converged and "best-possible" precision level. However, the position estimate may continue to move around due to whether the most recent data points have passed the validation gate or not. It is important to ensure that the validation gate is functioning properly to yield both a precise and accurate measurement in environments with high ambient noise or in longer distance surveys.

Chapter 5

Conclusions and Future Work

The Kalman filter provides a low-storage method of calculating the transponder position estimate. It is able to determine the covariance error ellipse with each estimate, and the resulting area of uncertainty. By linking the ASV state estimate with the transponder position estimate, the Kalman filter is able to utilize the trustworthiness of the GPS measurements to create a more accurate estimate for the transponder position. The Kalman filter also provides a validation gate for erroneous data in the case of noisier environments or effects of multipath when the one-way travel time data is received. The Kalman filter used in this paper is tuned to a low sea state propulsion model for the ASV, but it can easily be adapted for higher sea states that experience larger significant wave heights.

Finally, in terms of running the algorithms on board the ASV in real time, the Kalman filter would out-perform the least-squares method in terms of required memory needed to calculate a precise estimate. The least-squares method from Section 2.1.1 must utilize every previous survey point and run calculations on a matrix whose dimensions are growing with each newly accumulated data point. The Kalman filter, however, has pre-set matrix sizes that do not increase, and it only needs the most recently acquired data point to determine its new estimate.

This will not only save computational space on the onboard computer, but it will also ensure that the computational time does not increase to greater than the interval between GPS data receptions (at a frequency of 1 Hz).

It is clear that there is a relationship between the distance traveled around an arc and the resulting precision that the survey will yield. From this analysis, it is recommended that traveling at least 150 degrees around a circle will result in a minimal error ellipse and coincident area of uncertainty. Once this arc is achieved, the steady-state position error covariance matrix will not shrink any further unless a missed validation gate measurement is obtained. In this case, the covariance matrix will grow to capture the further uncertainty a missed measurement adds, and then the covariance will shrink again as more measurements are processed in the filter.

The idea of driving straight line transects instead of an arc proves to be useful in diminishing the time it takes for the full survey to be completed. It appears that traveling two legs of a square will yield similar precision estimates to traveling a 180 degree arc, however the precision appears to be scaled by the average distance the ASV is from the transponder. Extended range surveys will incur a larger area of uncertainty based off of the data available for this analysis. Future work will determine the relationship between the distance of the survey to the transponder and the resulting steady state area of uncertainty. It also appears that the abrupt turning, done by straight line transects, may impart some heightened area of uncertainty during the direction change, but this quickly levels out and returns to steady state again.

Further study would be needed to best determine the relationship between the shape of the survey and the resulting effect on precision. Also, the repeatability of the transponder location estimate could be better identified with several surveys done back to back to determine

if the same position was identified with each subsequent survey.

It is also noted that in this paper, the assumption that the speed of sound remains constant through the water profile works better for the December 2022 experimental setup, where depth only varies by 3 meters, than the August 2023 setup, where depth varies by over 20 meters between the transponder and the sub of the ASV. Future work could address how to better model the changing sound speed profile with depth. Here, the average of the sound speed taken from CTD casts was used for the August 2023 speed of sound constant used in Equation 1.1. Having a variable sound speed that affects the conversion of the one-way travel time into a pseudorange could potentially lead to higher accuracy in the final estimate of the transponder location.

The algorithm presented in this paper should implemented onboard an ASV to be able to conduct a fully autonomous survey of transponders after they are deployed. The use of a human-out-of-the-loop algorithm not only frees up personnel to focus on other matters of the mission, but it enables a form of communication between an AUV already deployed and the ASV used to perform the survey.

Appendix A

Environmental Conditions During Testing

The environmental conditions and bulk parameters of the sea state can be found in the figures below.

A.1   December 2022 Data Collection

Date data was collected: December 16, 2022

A.2   August 2023 Data Collection

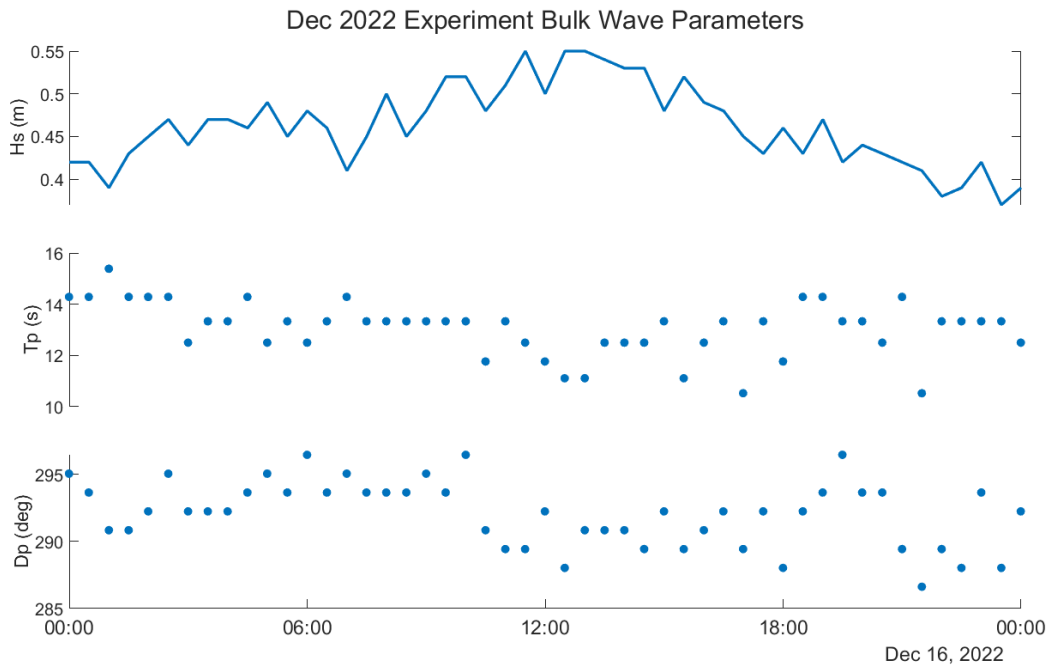Date data was collected: August 14, 2023

Figure A.1. Bulk parameters during the December 2022 data collection day
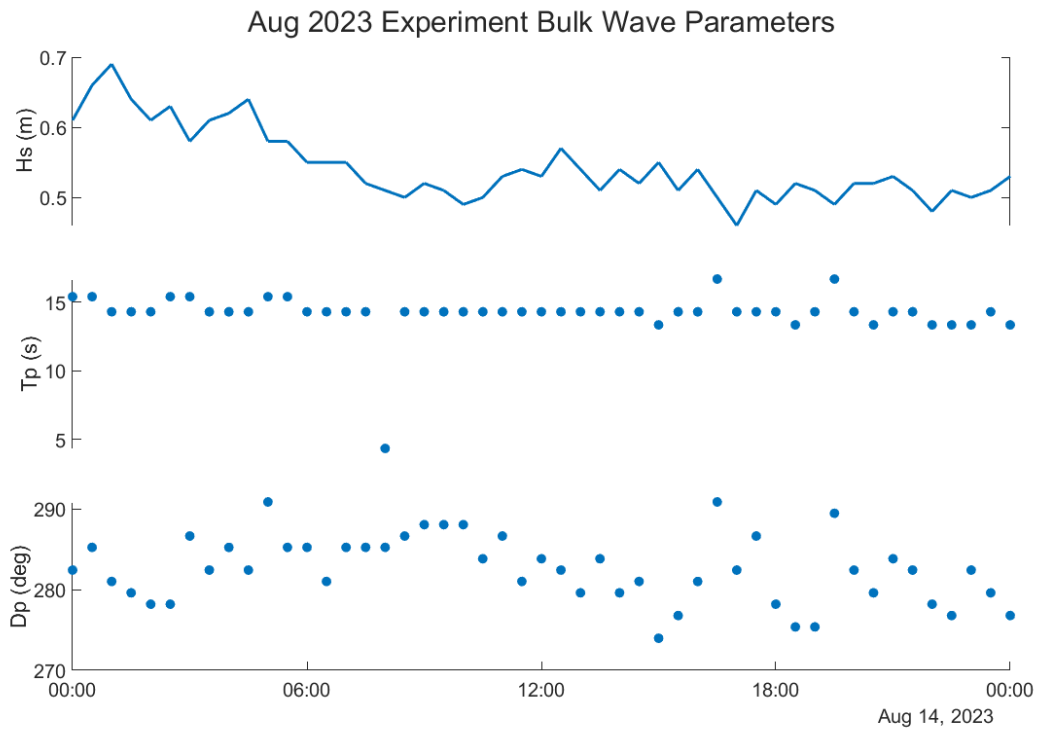

Figure A.2. Bulk parameters during the August 2023 data collection week
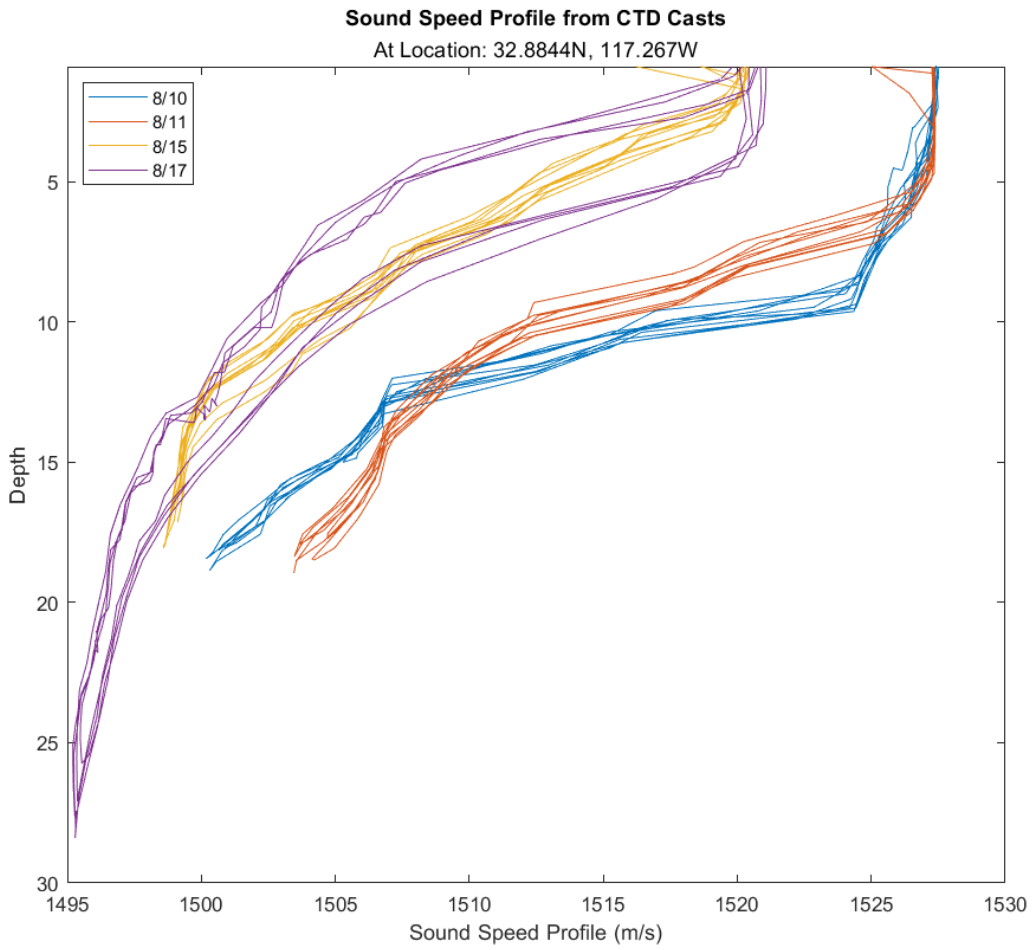
63

Figure A.3. CTD data converted into a sound speed profile for the week of testing in August 2023

Bibliography

[1] B. K. Evans, *The effect of coded signals on the precision of autonomous underwater vehicle acoustic navigation*. Thesis, Massachusetts Institute of Technology, 1999. Accepted: 2005-09-27T20:16:14Z ISSN: 4339-7344.

[2] C. J. Cassidy, *Navigation and target localization performance of the autonomous underwater vehicle REMUS*. Thesis, Massachusetts Institute of Technology, 2000. Accepted: 2005-09-27T20:11:18Z ISSN: 4794-1510 Journal Abbreviation: Navigation and target localization performance of the AUV Remote Environmental Measuring UnitS.

[3] I. Masmitja, S. Gomariz, J. Del-Rio, B. Kieft, R. O'Reill, P. J. Bouvet, and J. Aguzzi, "Optimal path shape for range-only underwater target localization using a Wave Glider," *The International Journal of Robotics Research*, vol. 37, no. 12, pp. 1447–1462, 2018.

[4] S. Xie, W. Hatfield, D. Price, D. Rimington, G. S. Sasagawa, J. White, and M. A. Zumberge, "Wave Glider-Based GNSS-Acoustic Surveying of a Single Transponder in Shallow Water," in *American Geophysical Union Fall Meeting*, (Chicago IL), 2022.

[5] E. Olson, J. J. Leonard, and S. Teller, "Robust Range-Only Beacon Localization," *IEEE Journal of Oceanic Engineering*, vol. 31, no. 4, pp. 949–958, 2006.

[6] F. N. Spiess, "Suboceanic Geodetic Measurements," *IEEE Transactions on Geoscience and Remote Sensing*, vol. GE-23, pp. 502–510, July 1985. Conference Name: IEEE Transactions on Geoscience and Remote Sensing.

[7] F. N. Spiess, C. D. Chadwell, J. A. Hildebrand, L. E. Young, G. H. Purcell, and H. Dragert, "Precise GPS/Acoustic positioning of seafloor reference points for tectonic studies," *Physics of the Earth and Planetary Interiors*, vol. 108, pp. 101–112, June 1998.

[8] U. Send, M. Visbeck, and G. Krahmann, "Aspects of acoustic transponder surveys and acoustic navigation," in *OCEANS '95 MTS/IEEE 'Challenges of Our Changing Global Environment'. Conference Proceedings*, vol. 3, pp. 1631–1642 vol.3, Oct. 1995.

[9] C. D. Chadwell, S. Webb, and S. Nooner, "Campaign-style GPS-Acoustic with wave gliders and permanent seafloor benchmarks,," in *Proceedings of the Subduction Zone Observatory Workshop*, (Boise Center, Boise, ID), Oct. 2016.

[10] T. Iinuma, M. Kido, Y. Ohta, T. Fukuda, F. Tomita, and I. Ueki, "GNSS-Acoustic Observations of Seafloor Crustal Deformation Using a Wave Glider," *Frontiers in Earth Science*, vol. 9, Mar. 2021. Publisher: Frontiers.

[11] B. Bingham, N. Kraus, B. Howe, L. Freitag, K. Ball, P. Koski, and E. Gallimore, "Passive and active acoustics using an autonomous wave glider," *Journal of Field Robotics*, vol. 29, no. 6, pp. 911–923, 2012. _eprint: https://onlinelibrary.wiley.com/doi/pdf/10.1002/rob.21424.

[12] A. Amador, S. T. Merrifield, and E. J. Terrill, "Assessment of Atmospheric and Oceanographic Measurements from an Autonomous Surface Vehicle," *Journal of Atmospheric and Oceanic Technology*, vol. 40, pp. 305–326, Mar. 2023. Publisher: American Meteorological Society Section: Journal of Atmospheric and Oceanic Technology.

[13] K. V. MacKenzie, "Nine-term equation for sound speed in the oceans," *Acoustical Society of America Journal*, vol. 70, pp. 807–812, Sept. 1981. ADS Bibcode: 1981ASAJ...70..807M.

[14] A. Amador, S. T. Merrifield, R. A. McCarthy, R. Young, and E. J. Terrill, "Wave Glider Speed Model for Real-time Motion Planning," in *OCEANS 2021*, (San Diego, CA), IEEE, Sept. 2021.

[15] S. T. Merrifield, J. Shapiro, R. Young, L. S. Laurent, H. Simmons, M. Otero, J. Hazard, E. Walsh, G. Gesireiech, and E. J. Terrill, "Autonomy system for USV/UUV coordinated sampling," in *OCEANS 2019*, (Seattle, WA), IEEE, Oct. 2019.

[16] A. Nehrorai, "Trilateration in Robotic Sensing Study Notes FL2010 Trilateration(what is) - ESE497 Wiki," Dec. 2010.

[17] K. Cheung, H. So, W.-K. Ma, and Y. Chan, "Least squares algorithms for time-of-arrival-based mobile location," *IEEE Transactions on Signal Processing*, vol. 52, pp. 1121–1130, Apr. 2004. Conference Name: IEEE Transactions on Signal Processing.

[18] J. Farrell and M. Barth, *The Global Positioning System & Inertial Navigation*. McGraw-Hill Education, 1999. Google-Books-ID: pdubAAAAMAAJ.

[19] G. Strang, *Linear algebra, geodesy, and GPS*. Wellesley, MA : Wellesley-Cambridge Press, 1997.

[20] D. J. Jwo, "Efficient DOP Calculation for GPS with and without Altimeter Aiding," *The Journal of Navigation*, vol. 54, pp. 269–279, May 2001.

[21] L. Kleeman, "Understanding and Applying Kalman Filtering," in *Proceedings of the Second Workshop on Perceptive Systems*, (Curtin University of Technology, Perth Western Australia), Jan. 1996.

[22] Y. Bar-Shalom, F. Daum, and J. Huang, "The Probabilistic Data Association Filter," *IEEE Control Systems Magazine*, vol. 29, Dec. 2009.